UNIVERSITY OF MIAMI

Observations of Meandering and Upwelling Events in the Agulhas Current at 34°S

By

Greta Leber

A DISSERTATION

Submitted to the Faculty
of the University of Miami
in partial fulfillment of the requirements for
the degree of Doctor of Philosophy

Coral Gables, Florida
May 2015

UNIVERSITY OF MIAMI

A dissertation submitted in partial fulfillment of
the requirements for the degree of
Doctor of Philosophy

OBSERVATIONS OF MEANDERING AND UPWELLING EVENTS IN THE
AGULHAS CURRENT AT 34°S

Greta M. Leber

Approved:

_____
Lisa Beal, Ph.D.
Professor of Meteorology and Physical
Oceanography

_____
Igor Kamenkovich, Ph.D.
Professor of Meteorology and Physical
Oceanography

_____
Donald Olson, Ph.D.
Professor of Meteorology and Physical
Oceanography

_____
M. Brian Blake, Ph.D.
Dean of the Graduate School

_____
Rick Lumpkin, Ph.D.
Oceanographer
Physical Oceanography Division
Atlantic Oceanographic and Meteorolog-
ical Laboratory
Miami, Florida

Leber, Greta M.   (Ph.D., Meteorology and Physical Oceanography)

Observations of Meandering and Upwelling Events   (May 2015)
 in the Agulhas Current at 34°S

Abstract of a dissertation at the University of Miami.

Dissertation supervised by Professor Lisa Beal.
No. of pages in text. (97)

Over three separate cruise, we collected direct velocity and hydrographic observations across the Agulhas Current at approximately 34°S. These transects included the first ever full-depth observations of a solitary meander. We use these data to explore how the solitary meander effects the transport, velocity structure and instantaneous water mass distribution of the current. Although we find that the meander is in geostrophic balance, the meander's fast propagation along the line causes sampling bias in the geostrophic velocities such that direct velocity measurements are necessary to observe the meandering current's structure. We find that the meandering current broadens and weakens, thereby maintaining its transport. The input of cyclonic vorticity during meandering causes thinning intermediate layers along the continental slope that also upwell 133 m onto the continental shelf at a rate of at least 13.3 m per day, but likely as much as 66.5-133 m per day. This process brings South Indian Central Water, normally found below the shelf break, up onto the continental shelf, which cools shelf waters by as much as 9°C. These changes coincide with the appearance of 0.25 fresher and 1°C cooler waters above and 0.25 saltier and 1°C warmer waters below the thermocline. We introduce a new coordinate system to separate these effects into diapycnal transport and kinematic effects due to the offshore shift and broadening of the current. We find that most of the temperature and salinity changes are due to diapycnal transport, although changes near the sur-

face are muddled by seasonal variability. Although theory suggests that cross-frontal mixing should be greater during a meander, we find that mixing across the front is not significantly enhanced. Hence, there are large diapycnal fluxes on either side of the front during a meander, while mixing across the front in inhibited.

Our data also include a wind-driven upwelling event that results in a similar magnitude cooling and uplift of South Indian Central Water. Therefore, we find that both upwelling-favorable winds and meandering can lead to cooling events with similar structure. We use satellite data to extend this analysis and identify cold events that are locally forced. Over an 11-year period, we identify an average of 4 events per year lasting 3.5 days. We consider upwelling-favorable alongshore winds, negative wind stress curl, meandering and increased current strength as possible forcing mechanisms. We find that all four forcing mechanisms significantly correlate to cold event length, and, with the exception of meandering, to cold event strength. We find that cold events are most likely to occur in austral summer and fall, during the time of year that prevailing winds are upwelling-favorable. Wind stress curl is found to be strongly dependent on meandering and alongshore winds. We find that frontal variability associated with meanders drives a local wind stress curl that further enhances upwelling. Wind stress curl is anticorrelated with alongshore winds and the two effects always oppose each other. 3 times more cold events are current-driven than wind-driven. Half of cold events are associated with meanders, one quarter with increased current strength, 18% with upwelling-favorable alongshore winds, and 5% with wind stress curl. One of the four forcing mechanisms explains 81% of cold event days and 93% of cold events.

To my husband and son: you are my inspiration and motivation.

Acknowledgments

I owe my sincere gratitude to many people for helping me complete this dissertation.

Firstly, I wish to thank my advisor and committee members: Lisa Beal, Igor Kamenkovich, Rick Lumpkin and Donald Olson. I appreciate their insight, honesty and support. In particular, I am so thankful that I chose Lisa Beal as my advisor. Her tough love, and never-ending support and guidance has been instrumental to my success.

I would also like to thank all of the professors that I have had at RSMAS. Their enthusiasm and dedication helped cement my decision to enter the field of Oceanography.

I want to thank all of my classmates who entered MPO in the fall of 2009. Thank you for your friendship and support these last several years.

Thank you to the Agulhas Group: Shane Elipot, Dian Putrasahan, Yu Cheng, and Joni Lum. Your enthusiasm and insight at weekly meetings was invaluable.

I want to thank all those that I met and worked with at the University of Cape Town. Thank you for making me feel welcome in your beautiful country. In particular, thank you to Benita Maritz who made South Africa a true home away from home.

Thank you to the RSMAS mooring team: Adam Houk, Mark Graham, and Robert Jones, as well as the crews of the R/V Knorr and Melville.

This work would never have come to fruition without your hard work during research cruises and completing data processing.

I want to thank my officemates: Teddy Allen, Peng Wang, Joni Lum, Changheng Chen, Gustavo Mastrorocco Marque, Jean Mensa and Ting-Chi Wu. Your support, kind words and friendship made for a great work environment.

I am lucky to have a long list of friends, without whom, my time in Miami would have been very difficult. In particular, thank you to the board gaming group: Ting-Chi Wu, Dian Putrasahan, Adam Houk, Nati Salvato, Milan Curcic, Joni Lum, Lucas Laurindo, Changheng Chen, and Honghei Zhang.

Thank you to all my long-distance friends up north in Maine. Although I don't see you all as much as I'd like, you are always willing to take time to see me when I'm visiting. I'm grateful for your continued friendship. In particular, thank you to Sarah Morrissey, Chad Waite, Kevin Merrill and Marie Merrill.

Finally, to my family. To my parents, thank you for your unending support through all my ups and downs. To my husband, thank you for all you have done to support this endeavor from being my audience for countless presentation practices, to helping me with programming issues, to listening to my frustrations. I know I couldn't have done this without you. Also, to my son Ellis, thank you for inspiring me to follow my dreams.

Contents

List of Figures

xvii

List of Tables

Chapter 1

Introduction

1.1 The Agulhas Current

1.1.1 Definition and Overview

The Agulhas Current (AC) is the western boundary current (WBC) of the southwest Indian ocean. Beginning around 27°S, the current flows south along the coast of Africa to the Agulhas Bank, where it retroflects to the east to become the Agulhas Return Current. The current is fed by eddies from the Mozambique Channel and south of Madagascar. As it flows southward, it also entrains interior waters. This entrainment increases the transport of the current as it travels downstream. At 30°S, Bryden et al. (2005) observed maximum velocities within the current's core of greater than 2 m s^{-1} and calculated a transport of 70 Sv ($1 \text{ Sv} = 10^6 \text{ m}^3 \text{ s}^{-1}$), making the AC the most energetic WBC in the Southern Hemisphere. Beneath the AC, the Agulhas Undercurrent (AUC) flows northeastward with a highly variable transport of 4.2 ± 5.2 Sv (Beal, 2009). At its retroflection, the current periodically sheds rings that transport warm, salty Agulhas waters into the South Atlantic. Agulhas rings are highly energetic and long-lived (Olson and Evans, 1986), allowing them to directly

modulate the strength of the Atlantic Meridional Overturning Circulation (Beal et al., 2011).

1.1.2 Velocity and Transport

Estimates of AC transport differ due to the current's latitudinal dependence, and variability. However, most studies agree that the AC has an average transport around 70 Sv. One of the earliest estimates for full-depth AC transport was calculated by Harris (1972) who used quasi-synoptic ship surveys off Durban to determine a current transport of 67 Sv. Gründlingh (1980) synthesized cruise data from 1975-1978 to calculate an average transport of 62 Sv at 31°S, and concluded that the current's transport increases 6 Sv per 100 km. From a year-long array at Port Edward (31°S), Bryden et al. (2005) calculated an AC transport that varied between 9 and 121 Sv and averaged 70 Sv. This led the authors to conclude that the AC is the strongest WBC in the Southern Hemisphere.

1.1.3 Eddies and Solitary Meanders

Lutjeharms et al. (1989) analyzed satellite data and concluded that shear-edge features, such as solitary meanders, eddies, and filaments, are present 65% of the time somewhere along the AC. The number of instabilities increases downstream. For example, one measure of solitary meander frequency is the distance that the current is found from the coast. Upstream of Port Elizabeth, the highly stable current is found within 20 km of the coast 90% of the time. This percentage falls to 28% near the Agulhas bank, due to frequent meandering (Lutjeharms et al., 1989; Gründlingh, 1983). Hydrographic data presented here is from 34°S: typically considered the border between the stable northern AC and more unstable southern AC (Lutjeharms, 2006).

1.2   Solitary Meanders

1.2.1   Definition and Overview

Throughout this work, we call the main instability of the AC a "solitary meander."
These features have several names throughout the literature: frontal waves, shear
(edge) eddies, pulses, and - most commonly - Natal Pulses (Gründlingh, 1992; Lutje-
harms et al., 1989; Lutjeharms and Roberts, 1988). The term "Natal Pulse" originated
because most solitary meanders form in the Natal Bight (between 28.5°S and 30°S).
In fact, de Ruijter et al. (1999) concluded that the Natal Bight was essential for
solitary meander formation because its gentler bottom slope destabilized the AC and
allowed the barotropic instability to grow. Tsugawa and Hasumi (2010) disproved
this using a high-resolution model where solitary meanders formed even without the
presence of the Natal Bight.

More recent modeling and observational studies agree that solitary meanders form
when upstream eddies from either the Mozambique Channel or south of Madagas-
car intersect the AC jet (Tsugawa and Hasumi, 2010; Rouault and Penven, 2011;
Schouten et al., 2002). The Natal Bight is simply the site where most of these ed-
dies interact with the AC, and its shallow slope is not necessary for solitary meander
formation. There is also no discernible difference between solitary meanders formed
outside of the Natal Bight and "Natal Pulses" (Gründlingh, 1992; Lutjeharms et al.,
1989; Lutjeharms and Roberts, 1988; Rouault and Penven, 2011; Tsugawa and Ha-
sumi, 2010). Thus, we choose to use the more general and dynamically descriptive
term "solitary meander" throughout this work.

Several studies describe the basic characteristics of AC solitary meanders. They
manifest as a cyclonic eddy inshore of the AC that propagates downstream within
the current (de Ruijter et al., 1999). They occur with no regular periodicity and

so estimates for their occurrence vary considerably from 1.6 (Rouault and Penven, 2011) to between 4 and 6 per year (Schouten et al., 2002; de Ruijter et al., 1999; Bryden et al., 2005). Solitary meanders push the AC core an average of 91-km offshore – but sometimes as much as 160 km or more (Rouault and Penven, 2011; Goschen and Schumann, 1990). On average, solitary meander phase speeds increase downstream from 10 to 20 km day^{-1} (de Ruijter et al., 1999; Rouault and Penven, 2011). But, solitary meanders may propagate faster than this, or decrease their speed as they travel downstream (Lutjeharms and Roberts, 1988; Rouault and Penven, 2011). The diameter of the inshore cyclonic eddy grows downstream from about 30 to 200 km (de Ruijter et al., 1999; Lutjeharms et al., 1989; Rouault and Penven, 2011; Lutjeharms and Roberts, 1988). Upstream of their crest, solitary meanders initiate secondary recirculations including: leakage (Lutjeharms et al., 2003); and instabilities that either merge with the initial pulse, detach from the current, or grow to become their own solitary meander (Rouault and Penven, 2011). Note that the downstream increases in both the diameter of the inshore eddy and the phase speed separate solitary meanders from traditional solitary wave theory. Solitary waves, also known as solitons, have a permanent form that is localized in space (Drazin and Johnson, 1989).

Solitary meander structure is overall baroclinic, with a large degree of vertical shear. However, their barotropic component is large since this vertical shear extends throughout the water column. Several studies confirm the significant barotropic component of these features. de Ruijter et al. (1999) analyzed energy availability in the AC and concluded that instabilities within the current are barotropic. Numerical simulations show that solitary meanders grow through barotropic energy conversion (Tsugawa and Hasumi, 2010). Observations confirm that the solitary meander creates

cyclonic velocity anomalies inshore of the current that reach throughout the depth of the water column (Lutjeharms et al., 2001).

The cyclonic anomaly, inshore of the current, connects to the AUC below causing the overall northeastward flow to vary strongly with solitary meander passage (Beal, 2009). The question of how and if meandering affects AC transport is less settled. Observations suggest that the current maintains its transport as it meanders: Beal (2009) found no change in current transport while meandering; and Bryden et al. (2005) found that the AC weakens as it moves offshore then strengthens at is maximum displacement - netting no overall change from its mean transport. Models, however, show AC transport peaks during meandering (Biastoch et al., 2009).

1.2.1.1 Dynamical Balance

The Rossby number, the ratio between the nonlinear and Coriolis forces, gives an idea of whether geostrophic balance should adequately describe a system. A Rossby number of 1 implies that the two terms have equal importance; a large Rossby number suggests the flow is highly nonlinear, and a small Rossby number means that the flow can be adequately described by geostrophic balance. In the case of a narrow (less than 50-km), swift (greater than 2 m s^{-1}) flow, such as a WBC, the Rossby number can be as large as 0.4, suggesting significant nonlinearity.

As a WBC, the AC's Rossby number can be fairly high, but previous studies agree that the AC is highly geostrophic. Beal and Bryden (1999) and de Ruijter et al. (1999) argue that the AC's along-stream velocity is geostrophic to first order. A separate study by Pichevin et al. (1999) argues that the AC should be geostrophic within 20%. However, these studies are based on a non-meandering AC. No analysis of ageostrophic flow within the meandering AC has been conducted because previous

observational studies have not collected concurrent direct and geostrophic measurements for comparison.

For a meandering flow, the largest ageostrophic term – the centripetal term – may become significant enough that it can no longer be ignored. In this case, the flow is best described by gradient wind balance. Johns et al. (1989) showed this was the case for the meandering Gulf Stream (GS). Though gradient wind balance better described the meandering GS's flow field, the authors stressed that the departures from geostrophy were small - no more than a 3% difference was found.

1.2.2   Regional and Climatic Influence

The solitary meanders of the AC are more than a dynamical curiosity; several studies confirm that they have broader implications both locally and globally. The AC, its retroflection region, and ring-shedding affect global climate by modulating the amount of inter-ocean exchange from the Indian to Atlantic oceans. As the largest and most energetic rings in the world ocean (Olson and Evans, 1986), Agulhas rings contribute a large amount of water to the surface "warm-water route" as defined by Gordon (1986). Several studies conclude that solitary meanders are able to directly trigger ring shedding events. Observational studies using satellites find several examples of this phenomenon (Lutjeharms et al., 2003; Rouault and Penven, 2011; Schouten et al., 2002). van Leeuwen et al. (2000) find a significant correlation between solitary meander genesis and Agulhas ring shedding events at a lag of 170 days for Geosat and 160 days for ERS 1/TOPEX/Poseidon. Penven et al. (2006) used a model to show that a simulation without Madagascar - and hence without Madagascar Channel eddies and Agulhas solitary meanders - lost its 100-day maximum in Agulhas ring shedding events.

The relationship between solitary meanders and ring shedding events may not be as clearcut as the above studies suggest. In a numerical simulation, Pichevin et al. (1999) defines two types of "pulses": "transport pulses," which increase AC transport within their vicinity; and "meander pulses," which are the classic solitary meanders that have been discussed here. The authors note that while "transport pulses" always result in Agulhas ring shedding events, "meander pulses" only cause a shedding event when the retroflected current is almost closed. Contrary to the Penven et al. (2006) modeling study, a second modeling study by Biastoch et al. (2008) showed that a simulation without solitary meanders did not affect the amount of inter-ocean exchange. The discrepancies between the modeling and observational studies may be due to the difficulty of simulating the highly turbulent AC region, where models are largely affected by their numerical choices (Backeberg et al., 2009).

This question becomes even more important within our changing climate. A warming climate is expected to increase the number of solitary meanders (Lutjeharms and De Ruijter, 1996). The process through which this occurs is outlined by the schematic in Figure 1.1. Briefly, under current climate change scenarios the strength of the westerlies is predicted to increase, which would in turn make the South Equatorial current more unstable causing more East Madagascar eddies and finally more solitary meanders. Assuming an increase in solitary meanders translates to an increase in Agulhas ring shedding events, then a warming climate is likely to increase the number of rings generated at the retroflection region. Since the strength of the Atlantic Meridional Overturning Circulation (AMOC) is expected to decrease with climate change, a subsequent increase in Agulhas ring shedding events may cause an increase in Agulhas leakage that helps to offset this change (Beal et al., 2011).

As previously stated in Section 1.2.1, the AUC varies strongly with the presence of solitary meanders. In a high-resolution modeling study, Biastoch et al. (2009)

shows that the transport of the AUC is significantly reduced in a model run lacking upstream perturbations and hence, solitary meanders. Though the AUC is defined as northeastward velocity below 1000 m, this reduction is likely related to the strong countercurrent that is generated inshore of the solitary meander at the surface (Lutjeharms and Roberts, 1988). This counter current is present inshore of every observed solitary meander, reversing the flow at the AC's mean location (Rouault and Penven, 2011).

The combination of the countercurrent affecting the shelf circulation inshore of the meandering current, and the AC being pushed offshore has several regional consequences (Gründlingh, 1992; Lutjeharms and De Ruijter, 1996). Jury et al. (1993) showed that coastal rainfall is heavily correlated with the AC's distance from the coast. When the AC is along the slope, rainfall is highest, and when it meanders, rainfall is much lower. Additionally, several studies have concluded that biological organisms - including fish and sea turtles - use the circulation of the AC to set their migration patterns (Beckley and Van Ballegooyen, 1992; Garratt, 1988; Heydorn et al., 1978). As such, solitary meanders are able to alter the pathways of these organisms.

It is clear that the localized effects of solitary meanders are not as well known as their global influence. We will discuss in the next section some of the important ways that meanders in other WBCs have been shown to effect the local, instantaneous water mass distribution with important consequences for biological productivity, and mixing of pollutants from coastal runoff. These effects have not been elucidated for Agulhas solitary meanders due to a lack of observations.

1.3   Water Masses

1.3.1   Water Masses of the Indian Ocean

Valentine et al. (1993) showed that the Indian Ocean is warmer and saltier than the average world ocean. This above average saltiness is due mainly to injection of saline Red Sea water at intermediate depths, and an excess of evaporation over precipitation. Because the Indian basin gains heat on average from the atmosphere, it converts cool surface waters to warm thermocline waters (Toole and Warren, 1993). Essentially, surface waters, salty from evaporation, are carried north by the interior circulation where surface warming and excess precipitation cover the high-salinity water with warm, lower salinity water - creating a salinity maximum at depth (Warren, 1981).

1.3.2   Water Masses of the Agulhas Current

The principal water masses of the AC, as defined by their neutral density, are: tropical surface water (TSW, $\gamma < 25.5$); subtropical surface water (STSW, $25.5 < \gamma < 26.4$); Antarctic Intermediate Water (AAIW) and Red Sea Water (RSW; $27.0 < \gamma < 27.92$); and North Atlantic Deep Water (NADW, $\gamma > 27.92$) (Valentine et al., 1993; Beal et al., 2006). The surface waters (STSW and TSW) form as described in the previous section; with STSW representing the salinity maximum at depth, and TSW the fresher layer along the surface (Toole and Warren, 1993). At intermediate depths, AAIW is recirculated from the south, while high salinity RSW flows southward from the Red Sea basin (Beal et al., 2006). At depth, NADW flows northward, below the AC in the AUC (Toole and Warren, 1993; Beal et al., 2006). Of a 65 Sv net AC transport, Stramma and Lutjeharms (1997) determined that 35 Sv came from the southwest Indian subgyre, 25 Sv came from east of Madagascar, and 5 Sv came from the Mozambique current.

Within the current, intermediate water masses to either side of the AC front are disparate: RSW is found inshore, and AAIW is found offshore of the current core (Darbyshire, 1966; Harris, 1972; Toole and Warren, 1993; Beal et al., 2006). Beal et al. (2006) concluded that, in general, water masses of northerly origin (RSW and TSW) are found inshore of the current core, while those of southerly origin (AAIW, STSW) are confined to its offshore side. Below this level, NADW is found on both sides of the current core. The next section will discuss how this water mass distribution within the AC is likely to be affected by the meandering current.

1.3.3 Water Mass Redistribution by Solitary Meanders

1.3.3.1 Cross-Frontal Mixing and Diapycnal Transport

The effect of solitary meanders on the instantaneous water mass distribution of the AC region has not been previously studied. However, several studies have analyzed the redistribution of water masses by meanders within other WBCs. These studies show that meanders in other WBCs are able to mix waters both on either side of the current front and across isopycnals, as well as upwell intermediate waters onto the continental shelf inshore of the meandering current.

Bower et al. (1985) showed that the mean Gulf Stream (GS) represents a barrier to mixing across its front. During meandering, however, Shaw and Rossby (1984) found that cross-stream velocities developed between 700 and 1300 m depth in the GS. Owens (1984) showed that this cross-frontal mixing occurs within meandering currents below the level at which the propagation speed of the solitary meander equals the current speed, the so-called kinematic steering level (KSL). Meanders raise the KSL, decreasing the depth at which water particles can cross current streamlines.

In addition to increasing cross-frontal mixing, Rodríguez-Santana et al. (1999) showed that GS meanders induce diapycnal transport. Using expendable bathyther-

mographs, Rodríguez-Santana et al. (1999) found intense mixing of surface and thermocline waters during the formation of GS meanders. In particular, meanders increased diapycnal shear, which the authors attribute to the growth of instabilities within the jet. However, this phenomenon has not been well studied and remains an active research question.

1.3.3.2 Upwelling

Large coastal upwelling events can lead to exchange between continental shelf waters and slope waters. This process mixes disparate water masses and promotes biological productivity as nutrient-rich water is advected from the adjacent (deep) ocean onto the shelf (Atkinson et al., 1983; Miller and Lee, 1995). This exchange also provides a mechanism for mixing pollutants from coastal runoff offshore (Churchill et al., 1986).

Observational studies have shown coastal upwelling inshore of western boundary currents tends to be episodic, and is primarily fueled by eddies that develop when the currents become unstable and meander (Brandini, 1990; Castro and Miranda, 1998; Campos et al., 2000; Stabeno and Van Meurs, 1999; Gawarkiewicz et al., 2001; Okkonen et al., 2003). Numerical simulations document the importance of upwelling-favorable alongshore winds for this exchange (Castelao et al., 2004).

Brandini (1990) discovered that nutrient concentrations along the shelf of the Brazil Current peak when meanders are present. Campos et al. (2000) showed that this meander-induced exchange was able to bring intermediate South Atlantic Central Water (SACW) onto the continental shelf during the summertime, when winds are predominantly from the northeast. The authors theorized that it was the combination of both upwelling-favorable winds and meandering that led to shelf-slope exchange. While the upwelling-favorable winds induce offshore Ekman transport, Campos et al. (2000) show meanders induce upwelling along their trailing edge and downwelling

along its leading edge. This is related to the dual passage of cyclonic and anticyclonic features, which leads to confluent flows at the meander trough, and diffluent flows at its crest (Olson, 2002).

Castelao et al. (2004) concluded that while solitary meanders brought SACW up to the shelf break, upwelling favorable winds were necessary to close the circulation loop and bring SACW onto the shelf. More recently, Castelao and Barth (2006) showed that the wind stress curl can be just as important a contributor to upwelling as Ekman transport caused by alongshore winds. This phenomenon is not isolated to the Brazil Current as solitary meanders have also been shown to bring intermediate waters onto the continental shelf inshore of the GS (Flierl and Davis, 1993; Lee et al., 1981). No study to date has evaluated meanders and/or upwelling-favorable winds as forcing mechanisms for upwelling events in the AC.

1.4 Motivation and Overview of Current Study

The knowledge gaps concerning solitary meanders in the AC stem from a lack of high-resolution observations and accurate simulations. Previous observational studies are limited to measuring solitary meander surface characteristics using satellite data (Rouault and Penven, 2011), while others fail to capture the entire feature using floats (Lutjeharms et al., 2003) or moorings that do not extend the meander's entire width (Bryden et al., 2005). Modeling studies of the highly turbulent AC region are sensitive to their numerical choices (Backeberg et al., 2009), and have, thus far, disagreed with observations about some fundamental solitary meander characteristics. In particular, observations suggest that solitary meanders do not affect AC transport (Beal, 2009; Bryden et al., 2005), but models show that they represent peaks in transport (Biastoch et al., 2009). My second chapter addresses this discrepancy.

Meanders in other western boundary currents have been shown to have large consequences for local water mass distribution. In particular, meanders provide a pathway for mixing of disparate water masses across a current's front, and across isopycnals. Meanders also mix high-nutrient deep water onto the continental shelf, especially during periods of upwelling-favorable winds. As such, they provide a pathway for shelf-slope exchange that allows coastal surface waters rich with runoff and/or larvae to be advected offshore. The upwelling of nutrient-rich central waters may also promote local biological productivity. To date, no study has elucidated whether these effects are seen in the meandering AC. This again stems from a lack of observations of the temperature-salinity structure of the meandering AC. My third chapter addresses how solitary meanders in the Agulhas Current modulate the instantaneous water mass distribution of the current. In my fourth chapter, I use satellite data to extend my analysis of upwelling events inshore of the Agulhas Current and assess their forcing mechanisms and characteristics. My fifth, and last, chapter summarizes the main conclusions presented. For simplicity, chapters 2-4 are each written with their own background and data/methodology sections so that they can be read in any order and/or individually.
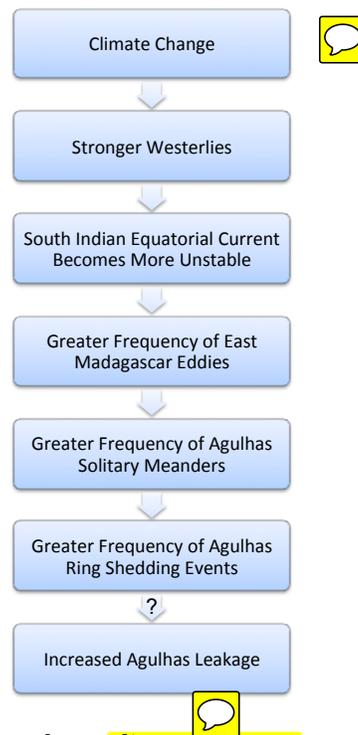
Figure 1.1: Schematic showing how <mark>climate change</mark> may be able to modulate the number of Agulhas solitary meanders. Though the last step is less certain, it suggests that <mark>climate change</mark> may increase Agulhas leakage through more ring shedding events caused by solitary meanders.

Chapter 2

Evidence that Agulhas Current transport is maintained during a meander

In this chapter, we discuss how solitary meanders in the Agulhas Current effect the current's transport and velocity structure. In April 2010, full-depth hydrographic and direct velocity measurements across a solitary meander in the Agulhas Current were collected at nominally 34°S. During a second cruise in November 2011 a transect across the non-meandering Agulhas Current was captured. These data provide the first full-depth, in-situ picture of the meandering Agulhas Current and allow us to investigate how the velocity structure and transport of the meandering current differs from its non-meandering state. An analysis of the horizontal momentum equations shows that the meander is in geostrophic balance. However, sampling bias causes large differences between geostrophic and direct velocity measurements during meandering, especially near the surface. As the current meanders offshore, its core speed weakens by more than 70 cm s^{-1} and its width broadens by almost 40 km. These two effects compensate so that the southwestward transport of the Agulhas current is largely unchanged during meandering. At the same time, the meander generates a strong inshore counterflow, which weakens the net Eulerian transport across the 300-km line by almost 20 Sv.

2.1 Background

The Agulhas Current (AC) is the strongest western boundary current (WBC) in the Southern Hemisphere with an average transport of 70 Sv (1 Sv = 10^6 m^3 s^{-1}) at 32°S (Bryden et al., 2005). North of approximately 34°S, the AC is relatively stable while attached to the South African continental slope. Once detached, the southern AC is characterized by frequent eddies, plumes and meanders (Lutjeharms and Connell, 1989). Solitary meanders (so-called Natal pulses) have been seen to form in the north and propagate the length of the current, connecting these two regions.

Solitary meanders are more than dynamical curiosities; they have broader implications both regionally and climatically. Meanders affect shelf circulation (Gründlingh, 1992; Lutjeharms et al., 1989), alter coastal rainfall patterns (Lutjeharms and De Ruijter, 1996; Jury et al., 1993), and significantly correlate with Agulhas ring shedding events (van Leeuwen et al., 2000). Agulhas rings transport water between the Indian and Atlantic oceans, carrying most of the so-called Agulhas leakage. This leakage of warm salty water forms the warm-water route of the thermohaline circulation as described by Gordon (1986). Several studies confirm the relationship between meanders and Agulhas rings (Schouten et al., 2002; Lutjeharms et al., 2003; Pichevin et al., 1999; Penven et al., 2006), suggesting that meanders are an important part of the climate system.

Solitary meanders manifest themselves as a paired inshore cyclone with an offshore anticyclone. The inshore cyclone is used to determine the meander's speed and size. These inshore cyclonic eddies typically have diameters between 30-200 km and propagate downstream within the current at 10-20 km day^{-1} (de Ruijter et al., 1999). Satellite observations show that meanders induce an inshore northeastward counter-current at the surface (Lutjeharms et al., 2001). Models show that this counter-current connects with the Agulhas Undercurrent (AUC) at depth (Biastoch

et al., 2009). The question of how meanders affect the full-depth velocity structure and transport of the current remains unknown. Model studies show that meanders increase AC transport (Biastoch et al., 2009), while a transport time series at 32°S showed AC transports reducing by 15-25 Sv during a meander (Bryden et al., 2005). Here, we present high resolution, full-depth, in-situ observations of a solitary meander within the AC. These are compared with observations of the non-meandering AC at the same latitude. We aim to understand how the velocity structure and transport of the meandering current differs from its non-meandering state.

2.2 Data and Methodology

Observations were collected across the AC at nominally 34°S (Figure 3.1, left). This paper presents data from four separate occupations of this line: two across the meandering AC in April 2010, and two across the non-meandering AC in November 2011. Data were collected using a CTD (Conductivity, Temperature, Depth), and lowered acoustic Doppler current profilers (LADCP). The LADCP configuration consisted of dual 300-kHz instruments during the April 2010 cruise, and a hybrid configuration, with 300 kHz upward-looking, and 150 kHz downward-looking instruments during the November 2011 cruise. The CTD system included a 12-bottle rosette, and a Sea-Bird SBE9-11 with an altimeter and dual temperature, conductivity and oxygen sensors.

The first CTD-LADCP line across the solitary meander was spread out over 9 days of mooring operations from 7-15 April 2010, and the second was sampled continuously over 3 days from 17-19 April 2010. We will concentrate on the second more synoptic line which we refer to as the meander line. Two further occupations of the same line were conducted in November 2011, the first collected over 10 days from 10-19 November 2011 during mooring operations and the second over 4 days from 20-23 November 2011. Again we concentrate here on the more synoptic dataset, which will

be referred to as the non-meander line. Each line of hydrographic data consists of 20 stations, with station spacing a minimum 6 km over the shelf and up to 24 km over deep water. Cast depths range from 50 m inshore to greater than 4500 m offshore (Figure 3.1, right). April 2010 data were sampled inshore to offshore, while November 2011 data were sampled offshore to inshore. Station locations for the meander and non-meander lines are labeled in the right panel of Figure 3.1: stations 21-40 for the meander line, and stations 31-50 for the non-meander line.

We use complementary satellite data to describe the surface characteristics of the solitary meander: sea surface temperature (SST) data from the group for high resolution SST (GHRSST), and mapped absolute dynamic topography (MADT) data from Archiving, Validation and Interpretation of Satellite Oceanographic Data (AVISO). The GHRSST product is a daily, 1.5-km resolution, gridded SST. The AVISO product is a daily, 1/3° resolution MADT. MADT is calculated as sea level anomaly plus a mean sea surface derived from altimetry, in situ measurements, and GRACE data (Rio et al., 2011).

2.3   Results

2.3.1   Meander Surface Characteristics

Rapidly changing SST and MADT fields coincident with our hydrographic occupations in April 2010 emphasize the dramatic effect of the passing meander (Figure 3.2a and b). Using the MADT data, we estimate that the inshore cyclonic anomaly that marks the solitary meander averages 100-km in diameter and propagates across the hydrographic line at 15 km day^{-1}. These estimates were acquired by using the 50-cm MADT contour to define the inshore cyclonic anomaly. We determined the diameter of the meander by approximating a circle using this contour. The meander's propa-

gation speed was determined by evaluating the period of time needed for this closed contour to propagate across our observation line. These values result in a propagation timescale of less than 7 days and are typical of previously reported Agulhas solitary meanders (so-called Natal Pulses) (Lutjeharms and Roberts, 1988; de Ruijter et al., 1999). The 7-day propagation timescale is comparable to the duration of occupation, which is 9 days for the first occupation and 3 days for our meander line.

The top panels of Figure 3.2 trace the development of the sea surface during the sampling of our asynoptic meander line. On April 7, the AC adjoins the continental slope, as evidenced by the large inshore velocity vectors, strong inshore MADT gradient, and warm inshore SST. There is also a clear region of diffluence along the observation line, concurrent with the passage of the solitary meander's trough. By April 11, the current core has moved to approximately 130-km offshore, creating an aliased double-core in the asynoptic in-situ velocity vectors. The inshore cyclonic eddy's leading edge abuts the hydrographic line, and a filament of warm water stretches into its center. By the end of the asynoptic meander line's collection, the crest of the solitary meander is only slightly upstream of our line. The maximum MADT gradient that marks the location of the AC weakens slightly as the inshore cyclonic eddy becomes more distinct.

The sea surface characteristics during meander line collection are shown in the middle panels (Figure 3.2b). Since the meander line was collected in just three days, it is more synoptic, but some changes are evident. The inshore cyclonic eddy propagates from slightly upstream to downstream of the line between April 17-April 20. The warm SSTs that mark the AC's core are noticeably cooler on April 20. The AC has narrowed, as compared to the top panels of Figure 3.2, consistent with confluence accompanying the passage of the solitary meander's crest.

For comparison, the sea surface characteristics during the non-meander line are shown in Figure 3.2c. Here, the AC is found directly against the slope in a narrow band whose path does not change over the course of the 3-day occupation. In conclusion, the non-meander line is highly synoptic, while data collection during the two meander lines was on timescales comparable to that of the propagating meander.

2.3.2 Sampling Bias

It is clear from the rapid evolution of the meander during the in-situ occupations that sampling bias could be a serious issue in this data set. To investigate this, we compared LADCP and geostrophic shear profiles from the meander line and found some large differences (Figure 2.3, top). These differences are greatest near the core of the meandering current: a difference as large as 150 cm s^{-1} is found 160 km offshore above 1000 m depth along the AC's offshore edge. In contrast, the bottom panel of Figure 2.3 shows that LADCP and geostrophic shears match well in the non-meandering current. Here the AC is in geostrophic balance, except at the surface where wind-driven Ekman velocities become important (Beal and Bryden, 1999). In this section, we look carefully at the attribution of the geostrophic departures in the meander line, which could be due in whole or part to sampling bias, ageostrophic acceleration of the flow around the meander, or measurement error. We first consider the amplitude of measurement error.

Random measurement errors are a product of LADCP inverse processing (Visbeck, 2002). In the meander line, these formal errors average ±11 cm s^{-1} throughout the domain. Large as they are, these errors cannot account for the geostrophic departures seen in Figure 2.3. For the non-meander line, measurement errors average ±7 cm s^{-1} throughout the domain. Since errors within each line are comparable, they cannot explain the differences in geostrophic departures between the meander

and non-meander lines. Moreover, Thurnherr (2010) show that true LADCP velocity errors are significantly smaller than these formal estimates. The strong agreement between geostrophic and LADCP velocity shear profiles in the non-meander line support this (Figure 2.3, bottom), and suggest that errors are likely small and random. Next, we consider ageostrophic flow as a possible explanation for the geostrophic departures in the meander line.

Gradient wind balance is considered the dominant balance for a flow that is accelerated around a radius of curvature such as the velocities in our meander line. This balance is given by:

$$v^2/R + fv = fv_g \tag{2.1}$$

where v is the gradient velocity (taken as LADCP), R is the radius of curvature, f is the Coriolis force and v_g is the geostrophic velocity. For the meander line, the gradient wind balance yields maximum ageostrophic velocities of order 15 cm s^{-1}. This value is a full order of magnitude too small to explain the differences seen in Figure 2.3. Next, we perform a full momentum balance analysis to further investigate ageostrophic flow as an explanation for the observed geostrophic departures.

In a rotated coordinate system, with x the alongstream or cross-track direction (rotated 64°, positive to the northeast) and y the cross-stream or along-track direction (positive inshore, to the northwest), the horizontal momentum equations are given by:

$$\partial u/\partial t + u\partial u/\partial x + v\partial u/\partial y + w\partial u/\partial z - fv = -\partial P/\partial x \tag{2.2}$$

$$\partial v/\partial t + u\partial v/\partial x + v\partial v/\partial y + w\partial v/\partial z + fu = -\partial P/\partial y \tag{2.3}$$

where f is the Coriolis term, P is pressure, u and v are the downstream and cross-stream velocities, z is the local vertical, and w is the vertical velocity. Eddy stresses are neglected. These terms, excepting the absolute pressure gradient, can be calculated using our direct LADCP velocities and some scaling arguments. We assume a quasigeostrophic approximation, so that the terms involving vertical velocity can be neglected compared to the horizontal velocity in both Equation (2) and (3). Since we are unable to measure it, we also assume that the downstream change in velocity is small and neglect $u\partial u/\partial x$ in Equation (2) and $u\partial v/\partial x$ in Equation (3). This is justified since we assume the downstream gradients are much smaller than the cross-stream gradients. We are left with the following equations for the alongstream and cross-stream horizontal momentum balance where every term on the left hand side is directly measurable from our data:

$$\partial u/\partial t + v\partial u/\partial y - fv = -\partial P/\partial x \qquad (2.4)$$

$$\partial v/\partial t + v\partial v/\partial y + fu = -\partial P/\partial y \qquad (2.5)$$

The local time derivative is calculated from the difference in u and v between each of the two occupations in April 2010 and November 2011 and dividing them by the time between occupations in a manner similar to Joyce et al. (1990). Since we expect the largest geostrophic deviations to be close to the surface, Figure 2.4 shows all terms averaged only over the top 150 m of the water column from the left hand side of Equations (4) (left panels) and (5) (right panels). For the meander line (Figure 2.4, top panels), the Coriolis term dominates everywhere in both the across- and along-stream momentum balances. The Coriolis term is 4 times larger than the inertial terms for the alongstream, and 15 times larger for the cross-stream balances. For the non-meander

line, the domination of the Coriolis term is similar except in the alongstream momentum budget within 50-km of the coast, which is dominated by the non-linear terms. This is on the inshore, cyclonic side of the current where the cross-stream shears are very large over the continental slope. Therefore, our momentum analysis suggests that the meander line is in geostrophic balance, since the unmeasured pressure gradient term likely balances the dominant Coriolis term in this case. Surprisingly, it is the non-meandering AC which shows a small departure from geostrophic balance, but only in the along-stream momentum budget, where acceleration is significant over the continental slope. Looking back at Figure 2.3, the large differences between direct (LADCP) and geostrophic velocities (cross-stream momentum balance) during the meander event are clearly not explained by geostrophic departures in the momentum balance of the flow. Most notably, there are no significant accelerations in the case of the meander, despite the curvature and rapid evolution of flow.

We now consider sampling bias as a possible explanation for the geostrophic departures in the meander line. As an integrated value, geostrophic velocities are particularly sensitive to the movement of sloping isopycnals during meandering. Depending on the length of occupation, this can lead to large sampling biases. Johns et al. (1989) quantify the fractional error in geostrophic velocities across a meandering current as the ratio between the current's lateral velocity, and the ship's cross-sectional velocity offshore. Hence, we calculate the fractional error of the geostrophic velocity as:

$$(|V_1 - V_2|)/V_1 = V_c/V_s \tag{2.6}$$

where $|V_1 - V_2|$ is the difference between our geostrophic and LADCP velocities, V_c is the current's lateral velocity as the meander advects across the line, and V_s is the ship's velocity along the sampling line. During meander passage, the AC's lateral velocity varies between about 16 and 26 km day^{-1}, as estimated from the movement

of the warmest SST contour along the observation line in the daily GHRSST data. The ship's average velocity along the line varies between 39 and 76 km day^{-1}, largely dependent on CTD sampling depth. Hence, the resulting fractional error due to sampling bias is between 21% and 67% of the geostrophic velocity. In the core of the meandering Agulhas current, velocities reach over 150 cm s^{-1}, implying a sampling bias up to 100 cm s^{-1}. This bias is large enough to explain the discrepancy we see in our geostrophic velocities from the meander line. The lateral motion of the current along our line during the meander event is comparable to the speed at which we can occupy the line and this distorts the horizontal density gradients from which geostrophic velocity is calculated.

2.3.3 Velocity Structure

We have shown that our geostrophic velocities are biased by the fast evolution of the flow during the meander line occupation. However, we can use direct velocities from LADCP to examine the velocity structure of the solitary meander. Comparing cross-track direct velocities from the meandering AC and the more common non-meandering case, shown in Figures 2.5a and 2.5b, reveals that the Agulhas current weakens and broadens as it meanders offshore.

During meandering, the AC core moves 89 km offshore from the 600-m isobath to the 4200-m isobath. (Figures 2.5a and 2.5b). This offshore shift significantly alters the circulation along the slope. During the meander, an inshore, strongly barotropic countercurrent develops at the typical location of the non-meandering AC's core. The along-track area of this northeastward countercurrent is two orders of magnitude larger than the northeastward flow during the non-meandering line (4×10^{-3} km^3 vs 0.3 km^3), which is restricted to below 1000 m as the Agulhas Undercurrent. The development of an inshore countercurrent during solitary meander passage is well-

established from the literature (Lutjeharms and Connell, 1989; Bryden et al., 2005). Here, we find that this anomaly reaches throughout the full depth of the water column, and occupies the space of the non-meandering AC core.

The development of an inshore countercurrent is reflected in the location and direction of isopycnal slopes. We use neutral density surfaces as defined by Jackett and McDougall (1997) and overlain in yellow on Figure 2.5 to illustrate these changes. The maximum neutral density gradient is found at 30 km when the Agulhas Current is attached to the slope, while it is found 120-km offshore when it is detached. Approaching the slope, the $\gamma = 27.92$ neutral density surface dips sharply downward for the meander line indicating northeastward flow. In contrast, the $\gamma = 27.92$ neutral density surface in the non-meander line dips gradually upward at the slope, indicative of the southwestward-flowing AC. The overlain neutral density contours also show a dramatic thinning of neutral density layers during meandering. This is especially apparent over the shelf, and along the slope between $\gamma = 26.4$ and $\gamma = 27$. This thinning of neutral density layers during the meander has large implications for the overall potential vorticity structure, as described in the next section.

Meandering of the AC is accompanied by a broadening and weakening of its core. Cross-track velocities weaken by 72 cm s^{-1} from -208 cm s^{-1} to -136 cm s^{-1}, and the current's width, defined by the outcropping of the -50 cm s^{-1} cross-track isotach, increases by 37 km, from 88 km to 125 km. We note that the meandering flow is also weaker in the local direction of flow, but we can approximate that its width may be similar. The maximum speed is 191 cm s^{-1} at a heading of 200 degrees T (45 degrees to the east of cross-track) for the meander and is 213 cm s^{-1} at a heading of 225 degrees T (15 degrees east of cross-track) for the non-meander line. Using these angles, we can approximate the width of the current (defined by the 50 cm

s^{-1} cross-track isotachs) in the local direction of flow in each case as 88 km in the meander and 85 km in the non-meander line.

To quantify changes in the structure of the current we calculate its relative vorticity, defined as the cross-stream gradient of the down-stream velocity $(\partial u/\partial y)$ measured at the surface. Note that given the angle of the meander flow to the ACT line, the relative vorticity could be as much as double this in the true local direction of flow. We find that the relative vorticity structure of the AC changes significantly during a meander. The amplitude of the inshore relative vorticity of the non-meandering current is more than three times greater than its offshore side: -1.9×10^{-4} s^{-1} vs. 5.7×10^{-5} s^{-1}, while for the meandering current relative vorticity on either side of its front is more comparable, -4.6×10^{-5} s^{-1} vs. 2.8×10^{-5} s^{-1}. In the next section, we explore the vorticity structure of the meandering current in more detail by calculating the full Ertel's potential vorticity (Pedlosky, 1986).

2.3.4   Vorticity Structure

To further explore the structure of the current, we calculate the full Ertel's potential vorticity. We find that differences in planetary vorticity dominate the total difference in cross-sectional potential vorticity structure between the meandering and non-meandering currents. Hence, the largest changes in total potential vorticity are due to variations in isopycnal layer thickness.

To calculate the full Ertel's potential vorticity (Q) equation (Pedlosky, 1986), we follow Beal and Bryden (1999) and rewrite Q such that all terms can be calculated using our CTD-LADCP data:

$$Q = Q_p + Q_{hs} + Q_{vs} = (fN^2)/g[1 + (1/f)(\partial u/\partial y) - 1/(N^2)(\partial u/\partial z)^2] \qquad (2.7)$$

where the total potential vorticity (Q) is shown as the sum of the planetary vorticity (Q_p), relative vorticity from horizontal shear (Q_{hs}), and relative vorticity from vertical shear (Q_{vs}). Note that again we neglect the downstream gradient when calculating the Q_{hs} term since our dataset limits us to cross-stream gradients only. Since the local direction of flow for the meander line is 45 degrees east of the cross-track direction, the unmeasured downstream gradient term could potentially double the calculated relative vorticity term. We find, however, that the relative vorticity term is small when considering the total potential vorticity such that this difference does not change our main results. The upper panels of Figure 2.6 show the total Q, as well as the components Q_p, and Q_{hs}. We exclude the Q_{vs} term because it is an order of magnitude smaller than the other two components. The reader interested in the full Q structure of the non-meandering current is directed to Beal and Bryden (1999).

The Q_p of the meander line looks remarkably similar to the total Q, because it makes up the bulk of the signal (Figure 2.6b). The meander Q signal saturates at the surface due to high stratification (Figure 2.6a). Q is largely homogeneous along isopycnal layers that don't outcrop, except between $\gamma = 26.5$ and $\gamma = 27$ where the magnitude of Q decreases offshore of the current core. Q_{hs} contributes significantly to Q above 250 m, where it alternates in the offshore direction from positive to negative and back to positive. The velocity contours reveal that the changes in sign of Q_{hs} correspond to the core of the northeastward-flowing countercurrent above the shelf break approximately 40-km offshore, and to the core of the meandering AC found approximately 130-km offshore. The Q, Q_p, and Q_{hs} of the non-meandering current have a similar structure, but are shifted inshore (e.g. Beal and Bryden, 1999).

The bottom panels of Figure 2.6 show the differences, meander minus non-meander, in Q, Q_p and Q_{hs}. Changes in Q_{hs} can be attributed to the input of cyclonic relative vorticity inshore of the meandering current. These changes are comparable in size to

changes in Q_p only over the top 150 m of the water column. The total change in Q is dominated by isopycnal layer thickness changes. The largest fractional differences in Q are positive and found along the continental slope. These positive changes are indicative of uplifting and thinning of isopycnal layers during the meander, associated with the cyclone inshore of the meandering current. A less significant positive difference 250-km offshore at 650-m depth can be attributed to a homogeneous region of low amplitude Q_p (Figures 6a and 6b) between $\gamma = 26.5$ and $\gamma = 27$ in the meander. This is Subantarctic Mode Water (SAMW) as described by Hanawa and Talley (2001). This SAMW signature is absent in the non-meander case. Since the meander line was collected in April and the non-meander line in November, this difference could be due to seasonality of SAMW in the region. In summary, below outcropping density layers which may be dominated by seasonal differences, the bulk of the difference in Q is due to thinning isopycnal layers over the continental slope during the meander. This is the result of enhanced cyclonic vorticity inshore of the current during a meander.

2.3.5   Volume Transport

A previous study based on one year of mooring data at 32°S showed that the transport of the Agulhas Current decreases up to 25 Sv during meander events (Bryden et al., 2005). However, the limited length of their mooring array means that transport may have been missed during offshore excursion of the current. Here, we are able to calculate the transport of the Agulhas Current using a line of stations that fully capture the displaced current. Volume transports are calculated as across-track LADCP velocities multiplied by the cross-sectional area between each station, ignoring bottom triangles. A new method for determining transport error estimates was derived by randomly setting a posteriori velocity errors from the LADCP linear inverse method

from Visbeck (2002) to be positive or negative. Once the errors were randomly set to be positive or negative, the total error was summed. This process was repeated until the average total error stabilized (approximately 1000 times). Total errors in transport for the AC, AUC and interior were summed separately. We assume each region is independent, so that the total transport error across the line was calculated as the square root of the sum of the squares of the errors for each region.

The results of our transport calculations are shown in Figure 2.7. The AC transport, defined as the total southwestward transport, is 120 ± 1.1 Sv for the meander and 125 ± 0.5 Sv for the non-meander lines. These transport values are larger than the 70 Sv mean calculated by Bryden et al. (2005) at 32°S, which is consistent with the known increase in transport downstream due to entrainment (Casal et al., 2009). The 5 Sv difference between our transport measurements is less than 20% of the standard deviation of the transport at 32°S (Bryden et al., 2005). Note that transport accumulates out to 250 km for both the meander and non-meander lines, confirming that the WBC transport is fully captured within our 300 km hydrographic line. The northeastward transport across the line increases more than threefold during meandering. This difference in northeastward transport, rather than a change in the transport of the AC, is responsible for a 20 Sv net Eulerian transport difference between the two lines.

The right panel of Figure 2.7 reveals that the transport per unit depth for each line are markedly similar. Hence, our results show that solitary meanders represent a lateral shift of the AC, with little change in the depth structure and transport of the current.

2.4 Summary

The transport of the meandering Agulhas current is conserved due to the compensating effects of the broadening and weakening of its core. The Eulerian transport, however, decreases substantially due to the development of an inshore countercurrent. This inshore countercurrent represents a barotropic change to the AC since the transport per unit depth is unchanged.

As the Agulhas current meanders, its velocity structure loses the asymmetry that is characteristic of its non-meandering state. When the AC is against the continental slope, the relative vorticity of its inshore side is much greater than its offshore side. During the meander, these values are more comparable. Differences in the potential vorticity fields of the meandering and non-meandering current are dominated by thinning isopycnal layers over the continental slope owing to the development of cyclonic vorticity inshore of the current during a meander.

There are significant differences between the geostrophic and LADCP profiles of the meandering current. However, careful analysis of the horizontal momentum equations confirms the meander is in geostrophic balance and that these differences are caused by sampling bias owing to the rapid evolution of the solitary meander compared to the occupation time. Therefore, LADCP measurements are essential to capture the structure of the meandering current.
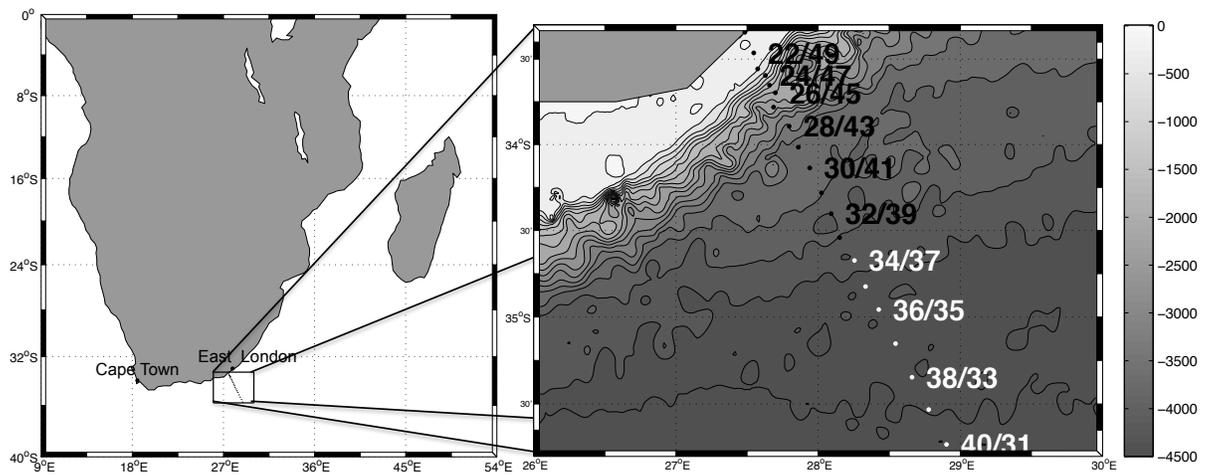
Figure 2.1: The left panel gives context for the geographic location of the observation line, located off the coast of southeast South Africa. On the right, contours represent the bathymetry (m) of the immediate area of the hydrographic lines using the colorbar on the right. Black and white circles mark hydrographic station locations. Every other station is labeled using the format meander line station number/non-meander line station number. Note that stations for each line are at the same geographic location, but are separated in time. Meander line stations increase inshore to offshore opposite to that of the non-meander line stations that increase offshore to inshore.
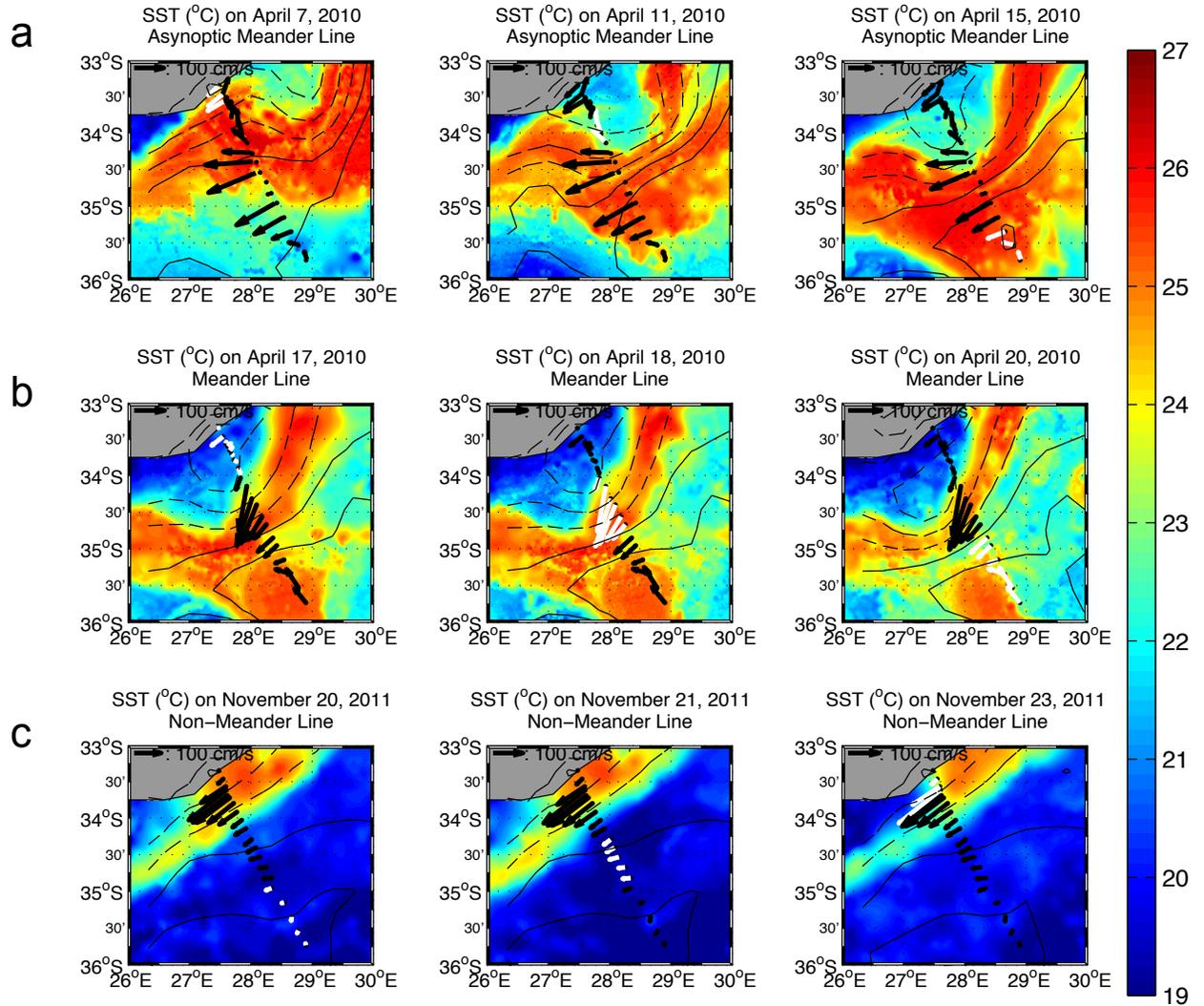
Figure 2.2: Nine panels showing the progression of the solitary meander during the first cruise (a,b) contrasted with the non-meandering current from the second cruise (c). Colors show sea surface temperature (°C) from GHRSST, with the color scale shown on the right. Black contour lines are mapped absolute dynamic topography (cm) from AVISO. 50 cm, 75 cm and 100 cm contours are dashed, while 125cm, 150 cm, and 175 cm contours are solid. Bold vectors show LADCP velocities averaged over the top 200 m from the asynoptic meander (a), meander (b) and non-meander lines (c), with velocity scale given by the arrow at the top left of each panel. White velocity vectors show the portion of the LADCP data that was sampled at the same time as the underlying satellite data.
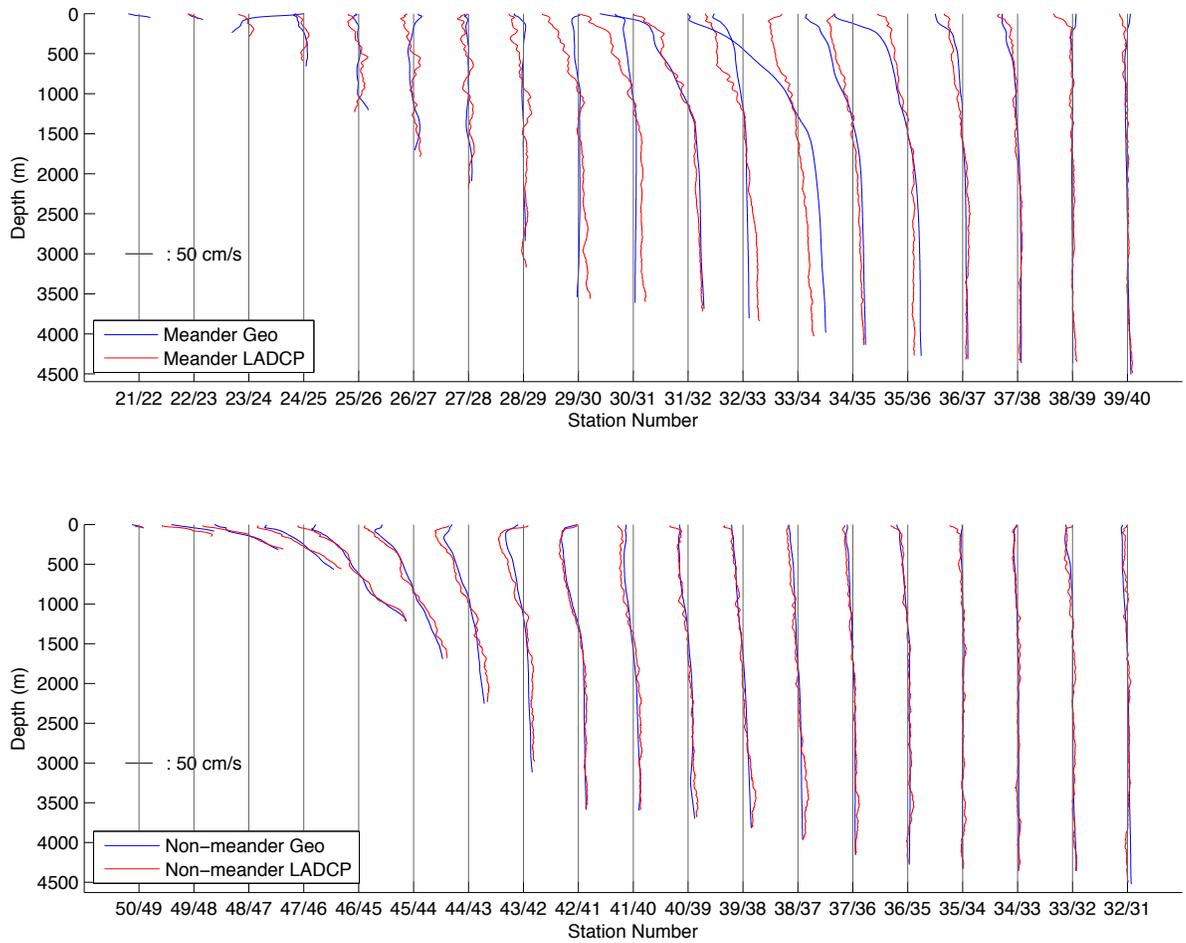
Figure 2.3: Top figure shows profiles of demeaned geostrophic velocity (blue) and LADCP velocity (red) for each station pair of the meander line, while the bottom figure shows the same for the non-meander line. A velocity scale is shown above the legend for each panel. Vertical grey lines represent zero velocity at each station.
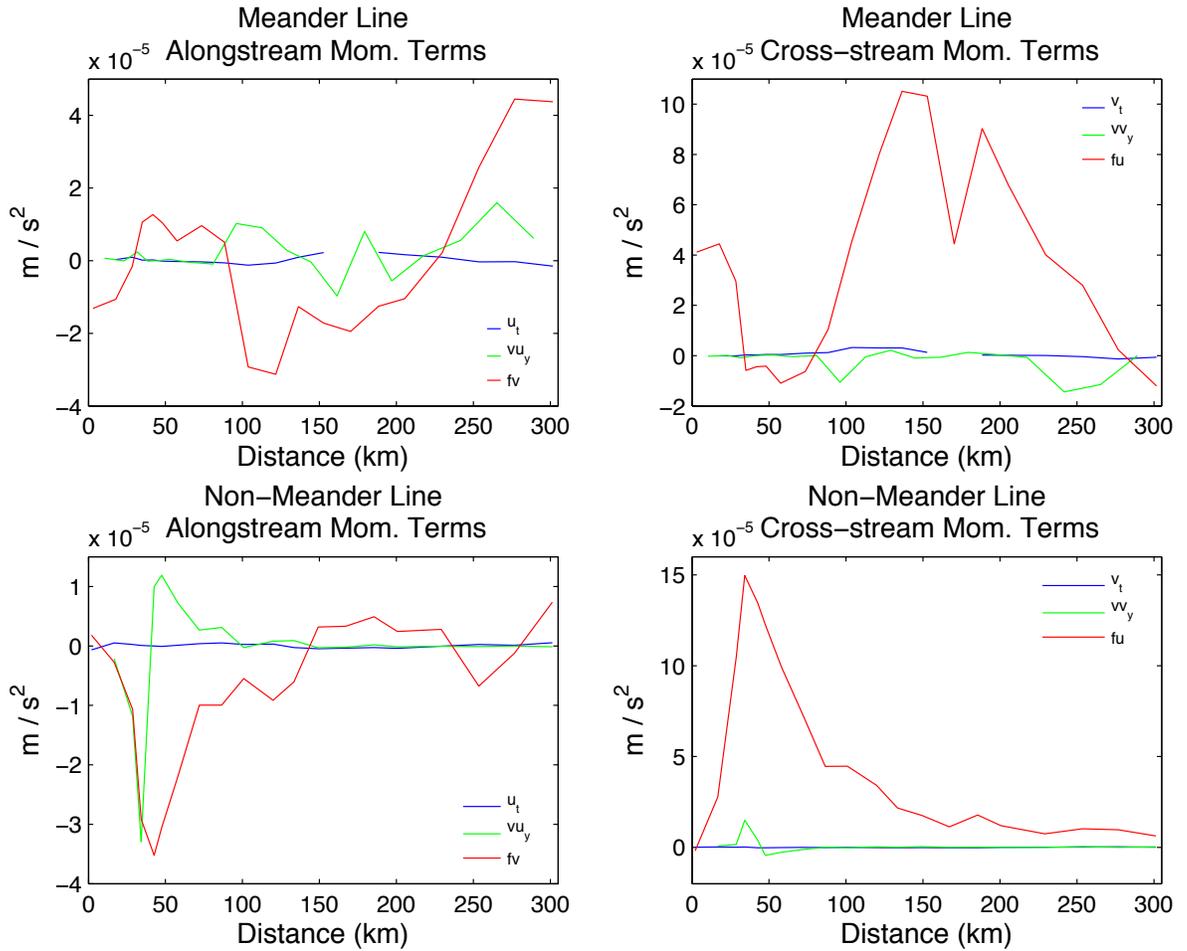
Figure 2.4: Horizontal momentum equation terms for alongstream (left panels) and cross-stream (right panels) balances for both the meander (top panels) and non-meander lines (bottom panels). The embedded legends within each panel identify each term as follows. On the left, the blue line is $\partial u/\partial t$, the green line is $v\partial u/\partial y$ and the red line is fv. On the right, the blue line is $\partial v/\partial t$, the green line is $v\partial v/\partial y$ and the red line is fu. Each term is averaged over the top 150 m of the water column and plotted versus distance from the coast along our observation line.
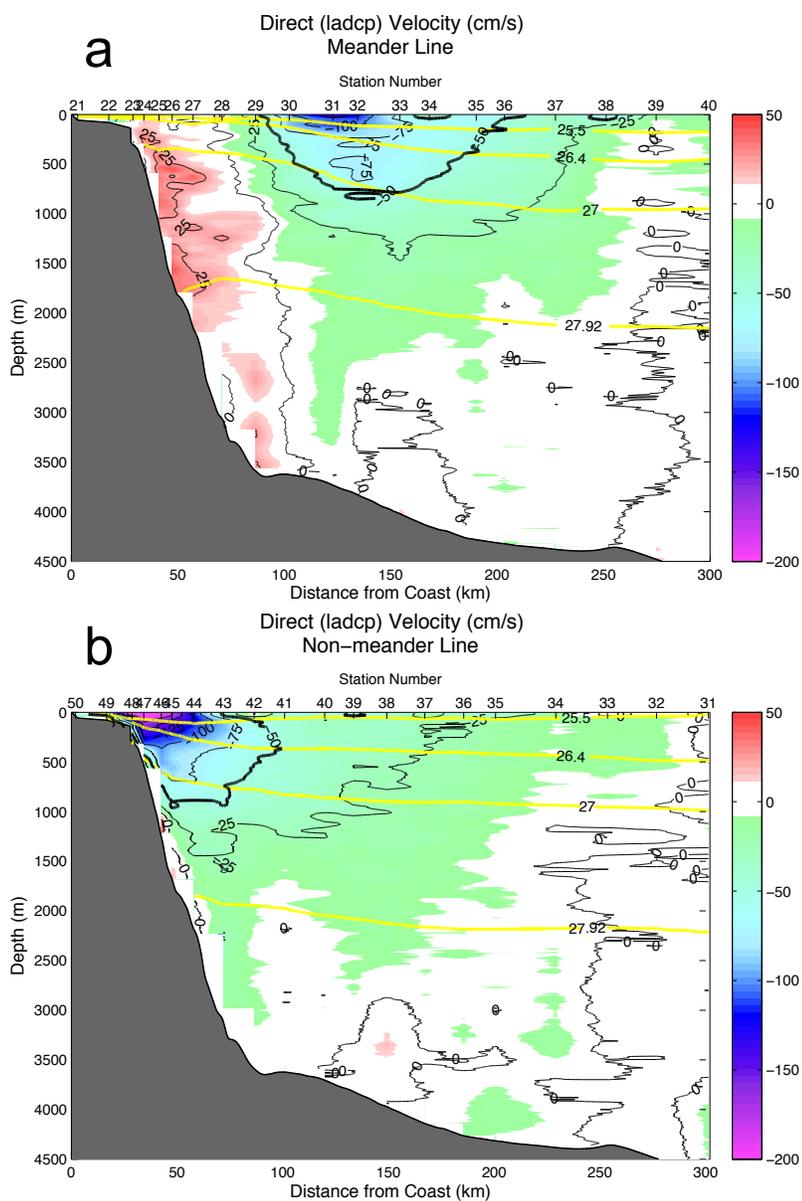
Figure 2.5: Direct velocity across the meander line (a) and non-meander line (b) from LADCP. Positive velocity (red) corresponds to northeastward flow, while negative velocity (green through magenta) corresponds to southwestward flow. Black contour lines of velocity in 25 cm s^{-1} increments from -175 cm s^{-1} to 25 cm s^{-1} are overlaid on top. The 50 cm s^{-1} contour discussed in the text is bold. Yellow contours of neutral density surfaces at $\gamma = 25.5$, 26.4, 27, and 27.92 are also overlaid.
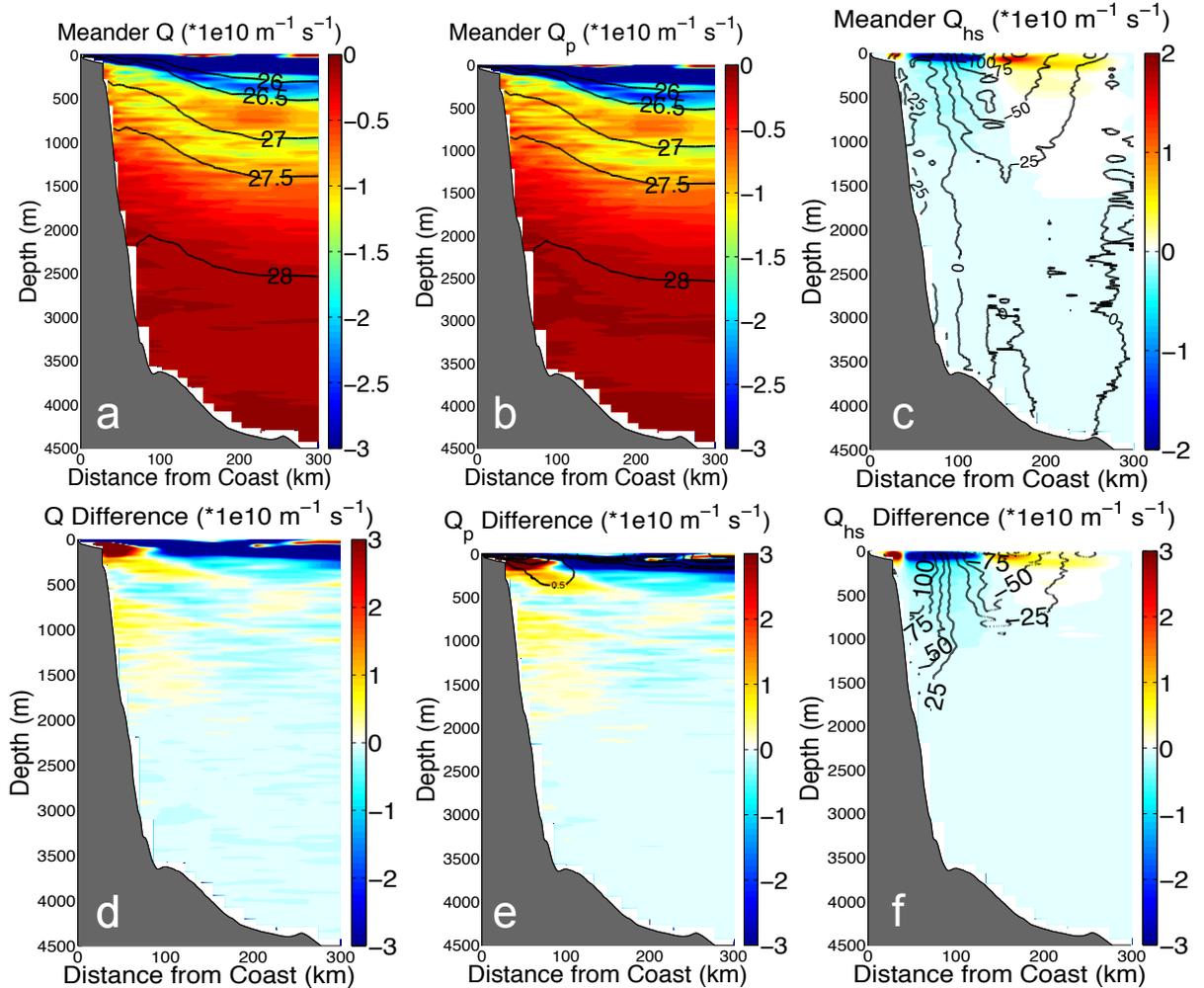
Figure 2.6: Colors show the potential vorticity components (excluding vertical shear) and total potential vorticity for the meander line (a-c), as well as the differences (meander minus non-meander; d-f). The calculation of the components and total potential vorticity is as described in the text. The meander total potential vorticity and planetary vorticity are overlain with neutral density contours from the meander line (a,b). The potential vorticity from horizontal shear is overlain with LADCP velocities from the meander line (c). In (e), the black contours show gamma difference in 0.5 kg m^{-3} increments (e). The vorticity from horizontal shear difference is overlain with LADCP velocity differences (f). All differences are given as meander line data minus non-meander line data.
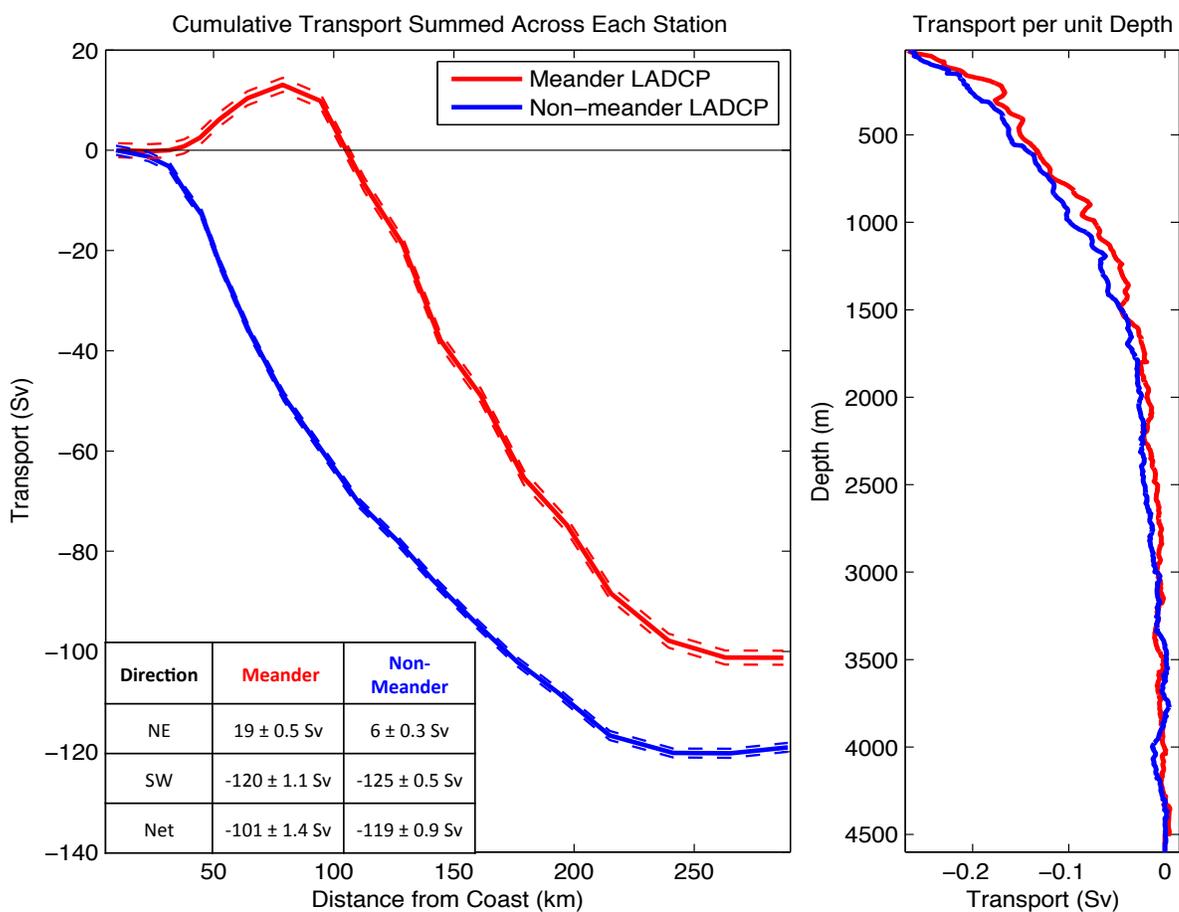
Figure 2.7: Left panel shows total cumulative transport (from LADCP) across the meander line (red) and non-meander line (blue) in Sv versus distance from the coast. The dashed lines give the error as described in the text. Total transport in each direction for each line are given in the embedded table. The right panel shows total transport per 2-m bins across the entire width of the meander (red) and non-meander (blue) lines.

Chapter 3

Local water mass modifications by a solitary meander in the Agulhas Current

In this chapter, we present full-depth hydrographic and velocity observations across a solitary meander within the Agulhas Current, and assess the degree to which the meander causes upwelling, cross-frontal mixing and diapycnal transport. These events can input nutrients onto the continental shelf as well as advect larvae offshore. We find that the meander drives inshore upwelling with vertical velocities of at least 13 m day^{-1}. The meander also causes diapycnal transport resulting in 1°C cooler and 0.25 fresher central waters and 1°C warmer, 0.25 saltier intermediate waters below the thermocline. We introduce a new coordinate system that separates these changes into kinematic changes due to meandering and property changes along transport streamlines. This reveals that most of the observed diapycnal transport below the thermocline is due to property changes. We find a small amount of enhanced cross-frontal mixing associated with solitary meanders of the Agulhas Current, but it is statistically insignificant. We believe this is due to the strongly barotropic nature of the meandering Agulhas Current, which maintains a deep steering level that inhibits mixing.

38

3.1 Background

Meanders are large deviations within the path of a strong current that are caused by barotropic and/or baroclinic instability (Tsugawa and Hasumi, 2010; Hansen, 1970). Observations have shown that Gulf Stream meanders cause enhanced cross-frontal mixing, diapycnal transport and upwelling. Bower et al. (1985) show that the mean Gulf Stream represents a barrier to mixing across its front, while, during meandering, Shaw and Rossby (1984) find significant cross-stream velocities between 700 and 1300 m depth. Rodríguez-Santana et al. (1999) showed that Gulf Stream meanders induce diapycnal transport of surface and thermocline waters during their formation. Gulf Stream and Kuroshio meanders can also upwell intermediate waters (for a review, see Olson (2001)). The ability of meanders to upwell intermediate waters has also been extensively studied in the Brazil Current (Campos et al., 2000; Aguiar et al., 2014). Due to a lack of observations, these processes have not been investigated for solitary meanders of the Agulhas Current (AC). For example, although Beal et al. (2006) showed that the AC represents a barrier to cross-frontal mixing, a lack of observations meant that the authors could only theorize that mixing would be enhanced during meander events.

The ability of solitary meanders to modulate water mass placement has local ramifications for both nutrient and pollution distributions (Huthnance, 1995). Large coastal upwelling events can lead to exchange between continental shelf waters and slope waters. This process promotes biological productivity as nutrient-rich water is advected from the adjacent deep ocean onto the shelf (Atkinson et al., 1983; Miller and Lee, 1995). This exchange also provides a mechanism for offshore mixing of pollutants from coastal runoff, as well as offshore larval transport (Porri et al., 2014). Since solitary meander events within the AC (so-called Natal Pulses) may occur up to 6 times per year, with large interannual variability in their frequency (Rouault

and Penven, 2011; de Ruijter et al., 1999), these effects may be especially important within the AC system.

Previous observational studies of solitary meanders in the AC at or above this latitude have been limited to surface characteristics using satellite data (Rouault and Penven, 2011), or sparse Lagrangian data using floats (Lutjeharms et al., 2003), or to moorings that miss a large portion of the meandering current (Bryden et al., 2005). More recent studies have considered interactions between the Agulhas Bank and the meandering AC further downstream, which is past the point where the AC generally separates from the coastline (Krug et al., 2014; Jackson et al., 2012). Here, we present high-resolution, full-depth, in-situ measurements of a solitary meander within the AC at 34°S. These are compared with data across the non-meandering current at the same latitude. This work follows and uses the same dataset as Leber and Beal (2014). We use these data to estimate the meander's effect on upwelling, cross-frontal mixing, and diapycnal transport.

3.2   Data and Methodology

For this study, we use data from four separate hydrographic transects each consisting of 20 stations collected during each of three cruises: two across the meandering Agulhas Current in April 2010, and two across the non-meandering Agulhas Current in November 2011 and in February 2013. Transect measurements were taken using a CTD (Conductivity, Temperature, Depth) and lowered acoustic Doppler current profilers (LADCP). The CTD package included a 12-bottle rosette and a Sea-Bird SBE9-11 with dual temperature, conductivity, and oxygen sensors plus an altimeter. For the LADCP configuration, a dual 300-kHz Workhorse monitor was used during the April 2010 cruise, and a hybrid configuration (300 kHz upward-looking, 150 kHz downward-looking) was used during the November 2011 and February 2013 cruises.

The four transects were collected at approximately 34°S (Figure 3.1). The first line collected in April 2010 was sampled over nine days of mooring operations from April 7-15 2010. We call this hydrographic line the asynoptic meander line. The asynoptic meander line contains stations 1-20, increasing offshore. The second April 2010 transect was collected over 3 days from April 17-19, 2010. We call this hydrographic line the meander line. The meander line consists of stations 21-40, increasing offshore. The third line was collected over 4 days from November 19-22 2011, and will be called the non-meander 1111 (for November 2011) line. The third line consists of stations 31-50, increasing offshore. The fourth line was collected over 4 days from February 15-18 2013 and will be called the non-meander 0213 (for February 2013) line. The fourth line consists of stations 1-20, decreasing offshore. Average station separation is 16 km, but ranges from a 5 km separation over the shelf to a 25 km separation offshore. Station depths vary between 50 m inshore to greater than 4500 m at the offshore end (Figure 3.1).

In addition to the hydrographic data, we use satellite imagery to detail the sea surface surface (SST) characteristics of the meander. We employ daily, 1.5-km resolution, gridded SST data from the group for high resolution SST (GHRSST). The GHRSST product is a Level 4 Multiscale Ultrahigh Resolution (MUR) gridded optimally interpolated dataset downloaded from the Jet Propulsion Laboratory (JPL) division of the Physical Oceanography Distributed Active Archive Center. Xie et al. (2008) show that this particular product has large errors close to the coast, especially in waters less than 40 m depth. Hence, we use the GHRSST product only to compare to our hydrographic data, whose shallowest station is 50 m.

3.3   Results

3.3.1   Meander Surface Properties

Satellite data allow us to determine the approximate timescale and magnitude of SST changes during the meander. Figure 3.2 gives a broad picture of the Agulhas Current meander of April 2010 that we captured with full-depth CTD and LADCP profiles. Over just two days, from April 9-11, inshore SST drops from 26°C to 21.5°C.

Figures 3.2a-d follow the development of the SST and surface velocities during occupation of the asynoptic meander line. The AC is recognizable by warm SST and large velocity vectors. The solitary meander can be identified as a region of high frontal curvature with cool waters inshore. On April 7, the Agulhas Current borders the coast, with an SST of 26°C 18 km from the coast (station 2). At the same time, offshore temperatures are as low as 21°C 302 km from the coast (station 20). By April 9, the AC is still found inshore but is much broader due to the offshore intrusion by the meander crest. Inshore SST 18 km from the coast (station 2) remains at 26°C, while temperatures 302 km offshore (station 20) have warmed slightly to 22°C. On April 11, the solitary meander has crossed the inshore portion of the hydrographic line. This coincides with cooling to 21.5°C 18 km from the coast (station 22). This change is corroborated by the hydrographic data; the average temperature of the top 20-m over the shelf falls 4°C between the asynoptic meander line and meander line occupations (Figure 3.3). Now the crest of the meander encompasses the entire hydrographic line and raises offshore temperatures to 25°C. By April 13, the crest of the meander is centered along the hydrographic line.

Leber and Beal (2014) used the diameter of the 50-cm contour of the inshore cyclone to classify this particular meander as 100-km in diameter. They tracked this contour to show that the meander propagates at approximately 15 km day^{-1}

across the line, resulting in a propagation timescale of just under 7 days. Note that these values are approximations since their altimetry product uses a six-week window for optimal interpolation. However, they are typical of previously reported solitary meanders within the Agulhas Current (so-called Natal Pulses, eg Lutjeharms and Roberts (1988)). The satellite fields during collection of the meander line and non-meander lines are shown in Figure 3.2e-g. The crest of the meander is situated directly along the meander line during its occupation, with the AC found 100 km offshore. In contrast, the AC is found directly against the continental slope during the non-meander lines, along a linear path that does not deviate during occupation. Next, we use the two meander lines to estimate upwelling within the meander over the shelf and slope.

3.3.2 Upwelling

Measurements taken at the inshore stations [1-8] of the asynoptic meander line capture the AC just prior to its being pushed offshore by the solitary meander (Figure 3.2a-b), while those taken at the same stations during the second meander line [21-28] capture the property field within the meander. Therefore, we can compare these inshore data to investigate solitary meander-induced changes over the shelf and shelf-break (Figure 3.3). We first present a simple scaling analysis to show that the temperature change is due to upwelling and/or horizontal advection. Our analysis then suggests that the vertical velocity of this meander-induced upwelling is at least 13.3 m per day, and perhaps as much as 133 m per day.

In this simple upwelling calculation, we make the assumptions that air-sea fluxes, diffusion and advection of offshore surface waters onto the continental shelf do not significantly contribute to the observed cooling. We conclude that the change in temperature is mainly due to upwelling, with additional contributions from horizontal

advection of cool Agulhas Bank waters. We consider the material derivative, $\frac{D}{Dt}$, of potential temperature, θ:

$$\frac{D\theta}{Dt} = \frac{\theta}{\rho c_p} + \frac{K_T}{\rho c_p}(\frac{\partial^2\theta}{\partial x^2} + \frac{\partial^2\theta}{\partial y^2} + \frac{\partial^2\theta}{\partial z^2}) \tag{3.1}$$

where ρ is the density of seawater, c_p is the specific heat capacity at a constant pressure, K_T is the thermal diffusion ratio, x is the alongtrack direction positive to the southeast, y is the cross-track direction positive to the northeast, and z is the vertical direction positive upwards. Assuming that air-sea fluxes and diffusion are small, then this simplifies to:

$$\frac{D\theta}{Dt} = 0 \tag{3.2}$$

This expands as:

$$\frac{\partial\theta}{\partial t} + u\frac{\partial\theta}{\partial x} + v\frac{\partial\theta}{\partial y} + w\frac{\partial\theta}{\partial z} = 0 \tag{3.3}$$

Close to the coast, our area of interest, the SST data confirms that there is no cross-track temperature gradient such that $\frac{\partial\theta}{\partial x} \approx 0$ (Figure 3.2a, 3.2b and 3.2e), so that the second term in Equation (3) $u\frac{\partial\theta}{\partial x} \approx 0$. With this argument, Equation (3) reduces to:

$$\frac{\partial\theta}{\partial t} + v\frac{\partial\theta}{\partial y} = -w\frac{\partial\theta}{\partial z} \tag{3.4}$$

At this latitude we cannot rule out the influence of advection in cooling waters close to the surface, represented by $v\frac{\partial\theta}{\partial y}$, since there is a pool of colder waters close by, over the Agulhas Bank to the south (Figure 3.2). Most of the cooling and uplift of isopycnals occurs in waters deeper than the continental shelf, which has a depth of 70 m along this line (Figure 3.3). Therefore, the primary cause of cooling must

be upwelling, or $w\frac{\partial \theta}{\partial z}$, associated with the meandering Agulhas Current. Satellite SST and in situ velocity data show that cool waters from the Agulhas Bank do not influence the upwelling meander region before April 11th. On April 7th we see warm SST and southwestward flow over the shelf between the two regions, reflecting the flow of the Agulhas Current away from the meander (Figure 3.2a). On April 9th, warm SST over the shelf suggests there is still southwestward flow, at least at the surface (Figure 3.2b). By April 11th the meander has propagated southward and the two regions of cooler waters have become connected by a small ribbon of flow next to the coast (Figure 3.2c). Subsequently, there is some additional cooling of SST in the meander trough (1-3°C, Figure 3.2c-e), which could be related to horizontal advection from the Agulhas Bank, or to a deepening of the meander trough, or most likely a combination of both.

In conclusion, most of the isopycnal uplift occurs offshore of the shelf break, in deep water, resulting from meander-induced upwelling. The 26.7 neutral density line uplifts by 133 m between the occupation of the two lines, which are ten days apart. This implies vertical velocities of at least 13.3 m per day and perhaps as much as 66.5-133 m per day, given the rapid, 1-2-day transition from the current into the trough at the line, as reflected by the SST data (Figure 3.2b and 3.2c). The latter estimate is comparable to observations further north in the AC region that suggest solitary meander-induced inshore upwelling is between 50 and 100 m per day (Bryden et al., 2005). Advection of shelf waters into the meander trough could account for another 1-3°C cooling at the surface (Figure 3.2c-e), and are likely the cause of the subsurface minimum in cooling seen over the shelf and shelf-break region between the two occupations (Figure 3.3).

3.3.3 Cross-Frontal Mixing

Previous authors have shown that surface and intermediate water masses within the non-meandering AC are disparate on either side of the current core with Red Sea Water (RSW) and Tropical Surface Water (TSW) found inshore and Antarctic Intermediate Water (AAIW) and Subtropical Surface Water (STSW) found offshore (Darbyshire, 1966; Harris, 1972; Toole and Warren, 1993; Beal et al., 2006). Below the intermediate level, North Atlantic Deep Water (NADW) is found on both sides of the current. This suggests that, in the mean, the front acts as a mixing barrier through intermediate depths. The mean Gulf Stream also represents a barrier to mixing across its front (Bower et al., 1985), but cross-frontal mixing has been observed during meandering (Shaw and Rossby, 1984). Cross-frontal mixing can occur below the level at which the propagation speed of the meander equals the current speed, the so-called kinematic steering level (KSL, Owens (1984)). Meanders raise the KSL in the Gulf Stream and enhance cross-frontal mixing at Intermediate depths. Our dataset allows us to investigate whether meanders in the AC induce similar enhanced cross-frontal mixing as predicted by Beal et al. (2006).

We define water masses using neutral density (γ) as follows: water masses with $25.5 < \gamma < 26.4$ are surface water masses, either STSW or TSW; water masses with $27 < \gamma < 27.92$ are intermediate water masses RSW and AAIW; below this is NADW. Within surface and intermediate layers, RSW and STSW have higher salinity than AAIW and TSW. Separations of surface STSW and TSW and intermediate AAIW and RSW are evident in both the meandering and non-meandering cases (Figure 3.4). In the case of the meandering current, salty STSW and fresh AAIW are pushed farther offshore with the current core, although a small parcel of RSW remains over the slope in the undercurrent.

To assess whether cross frontal mixing is enhanced during the meander, we follow Beal et al. (2006) and use relative vorticity, $\frac{\partial v}{\partial x}$ to identify water mass locations with respect to the AC front. Inshore water parcels have negative relative vorticity and offshore parcels have positive relative vorticity (Figure 3.5, for a full discussion of the vorticity structure of the meandering and non-meandering current, see Section 3.4 of Leber and Beal (2014)). The degree of frontal separation in both the meander and non-meander cases can be explored further by considering the overlap and maximum differences in distribution of water mass properties either side of the front (Figure 3.5).

In all cases, there is a greater overlap of water mass properties at the intermediate level (Figure 3.5b). This suggests that there is consistently more mixing at intermediate depth, where kinematic steering and potential vorticity gradients are weaker than at the surface. To quantify the differences in separation on either side of the current core, we calculate the maximum differences in the cumulative fraction distribution plots (Figure 3.5c). For both the surface and intermediate levels, the smallest difference in salinity distributions across the front is found in the meander line, suggesting cross-frontal mixing is enhanced by the meander. In particular, the intermediate level salinity for the meander line has the smallest difference and therefore shows the highest degree of mixing of any salinity group.

To test the significances of these differences, we employ two-sample Kolmogorov-Smirnov tests (Massey Jr, 1951) to determine the significance of the difference between the distributions (Figure 3.5c). Although the meander exhibits the greatest amount of mixing, the salinity distributions at each level in the meander are not significantly different from those of the non-meander lines (at the 99% level). We use Owens (1984) kinematic steering level (KSL) theory to explain why we see only a statistically insignificant greater amount of mixing in the meander.

In our case, the propagation speed of the meander, 15 km day^{-1} [17.4 cm s^{-1}], is matched by the current speed at 1320 m depth (Figure 3.4). Since the intermediate layer begins at approximately 500 m depth, this deeper KSL supports separation on either side of the current core at both the surface and intermediate levels. However, the intermediate layer extends to below 2000 m. Thus, the meander raises the KSL above the bottom of the intermediate layer. This may explain why we see more mixing at intermediate depths in the meander, but also why the increased mixing is statistically insignificant. We ultimately attribute the insignificance of the enhanced mixing to the meandering AC's strongly barotropic nature (Lutjeharms et al., 2001), leading to strong intermediate-level velocities that appear to support water mass separation regardless of meandering.

Although we can find no statistically significant enhanced cross-frontal fluxes during a meander, we do observe differences in water properties along neutral density surfaces between the meandering and non-meandering Agulhas Current (Figure 3.6). These could be attributed to kinematics as the current shifts offshore and broadens, or to property changes along streamlines. Looking at Equation 1, the latter can de due to local diapycnal fluxes related to the meander or to temporal changes, such as advection or air-sea fluxes, unrelated to the meander. We introduce a new streamwise coordinate system to separate the kinematics from true property changes.

During the meander, fresher, cooler waters appear in the sub-surface layer over the continental slope, while the intermediate layer becomes warmer and saltier (Figure 3.6b and 3.6c). Though temperature differences are not shown, they exhibit the same structure as salinity, with maximum changes of $\pm 1^\circ$C. At the same time, the thermocline thins by 50-100 m and uplifts 300-400 m (Figure 3.6a). Note that, unlike upwelling, these water mass changes involve differences with respect to isopycnals rather than the vertical movement of isopycnals. Hence, these changes are consistent

with diapycnal transport of waters out of the thermocline, both upward into the sub-surface layer and downward into the intermediate layer. However, they may be due to kinematic changes caused by the horizontal shift and broadening of the current, or to property changes along streamlines. Kinematic changes can be interpreted as Eulerian changes due to the current shifting in space. Property changes represent changes following the flow and include diapycnal transport directly induced by the meander as well as changes due to temporal variability. These can be separated using a streamwise coordinate system.

The assumption behind our new coordinate system is that AC transport is conserved during a meander. Leber and Beal (2014) found that as the Agulhas Current meanders offshore, it both weakens and broadens. These two effects compensate for each other so that the transport of the current remains the same. This allows us to interpolate properties onto lines of cumulative transport (Figure 3.7, bottom panels), and remove the combined effects of the broadening and offshore shift of the meandering current. Instead of considering properties with respect to distance from the coast, our new coordinate system linearly interpolates properties with respect to cumulative transport, beginning at zero at the coast and accumulating in the offshore direction. Figure 3.7 compares the LADCP velocities in the traditional distance from coast representation with the new cumulative transport streamwise system for the meander and non-meander 1111 lines. In the distance from coast representation, a highly barotropic countercurrent is clear inshore of the meandering current, which is broader and weaker than the non-meandering current. In the cumulative transport streamline representation (Figure 3.7, bottom panels), the cores of the current appear at almost the same streamline and the width of the current is similar. We believe this to be an improvement over a more typical streamwise coordinate system that

simply aligns current cores, since our coordinate system also allows for broadening of the current.

Property differences in our two coordinate systems are shown in Figures 3.6 and 3.8. The uplift and thinning of the thermocline, as illustrated by the changes in depth and thickness of neutral density layer 26.4-27.0 is striking in the Eulerian frame (Figure 3.6a), while it is removed in our stream coordinates (Figure 3.8a), revealing that the thermocline has in fact slightly thickened between the non-meander case and the meander line. In the distance from coast representation, the meander's thermocline is more than 150 m thinner than either non-meander line at the shelf break. In the cumulative transport representation, the meander's thermocline is now at least 25 m thicker than either non-meander line at the -20 Sv streamline. Likewise, the aforementioned water mass changes above and below the thermocline are shown to be largely forced by kinematics (Figures 3.6b-c and 3.8b-c), although there remain significant salinity changes close to the coast above the thermocline and everywhere within the intermediate layer (>0.15), related to property changes along streamlines (Figure 3.8b-c).

In sequential meander and non-meander property fields, these property changes would reflect diapycnal transport induced by the meander. However, since our datasets are eighteen months apart, property changes could be due in part to temporal changes in water mass properties. For instance, cooling and freshening above the thermocline only occurs between the meander (April) and the non-meander liner from November (Figure 3.8b). There are no clear changes above the thermocline when comparing the meander to the February occupation (Figure 3.8c). Hence, we attribute these changes to temporal variability, rather than to the meandering. In fact, the differences are consistent with expected seasonal changes, with cooler and fresher surface waters at the beginning of austral summer in November, and warmer waters towards the end

of summer in February. Below the thermocline, within the intermediate layer, water mass changes are evident in both comparisons, suggesting there are diapycnal fluxes here driven by the meander. Yet, the patterns of change are rather different, with a warming throughout the layer in one case and a pattern of warming above cooling in the other. Below the thermocline, property changes explain greater than 60% of the observed differences between the meandering and both non-meandering cases (Figure 3.9). Hence, we can conclude that property changes below the thermocline are dominated by diapycnal transport caused by the meander.

3.4   Summary

We find that the passing meander is associated with a drop in sea surface temperature of 5°C over two days along the continental shelf. Our in-situ data shows that this drop in temperature coincides with a 133-m upwelling of intermediate-level isopycnals at a rate of at least 13.3 m per day, but likely as much as 66.5-133 m per day. Compared to upwelling eastern boundary currents, these latter estimates for vertical velocities are short-lived but large. Upwelling of 66.5 m per day would be more than twice the vertical velocities observed in the Benguela current (26 m per day) and are comparable to those observed in the Canary Current (86 m per day) (Merino et al., 2004).

The meander causes about 0.25 freshening and 1°C cooling above the thermocline and an increase in salinity and warming of the same magnitude below the thermocline. To determine the extent to which these changes are caused by diapycnal transport induced by the meander, we introduce a new coordinate system that separates the kinematic effect of the shifting and broadening current from property changes along transport streamlines. We find that the meander induces diapycnal transport below the thermocline, and probably also above, although near-surface results are muddled by seasonal variability between transects.

Unlike the Gulf Stream and contrary to expectations, we find that the solitary meanders of the Agulhas Current do not significantly enhance cross-frontal mixing. It is possible that our results cannot be generalized and future research is needed to determine whether smaller or larger meander events significantly enhance mixing, or whether mixing is dependent upon the development stage of the meander. The reason for the lack of enhanced mixing, in this case, is attributed to the vertical structure of the Agulhas Current, with deep-reaching velocities that lower the kinematic steering level and inhibit cross-frontal mixing regardless of meandering. Our streamwise analysis suggests that there is enhanced diapycnal fluxes during a meander, while the relative vorticity analysis suggests cross-frontal fluxes are not significantly enhanced. This implies that the meandering AC is enhancing mixing in the cross-frontal direction on either side of the current, even though mixing across the current core is suppressed.
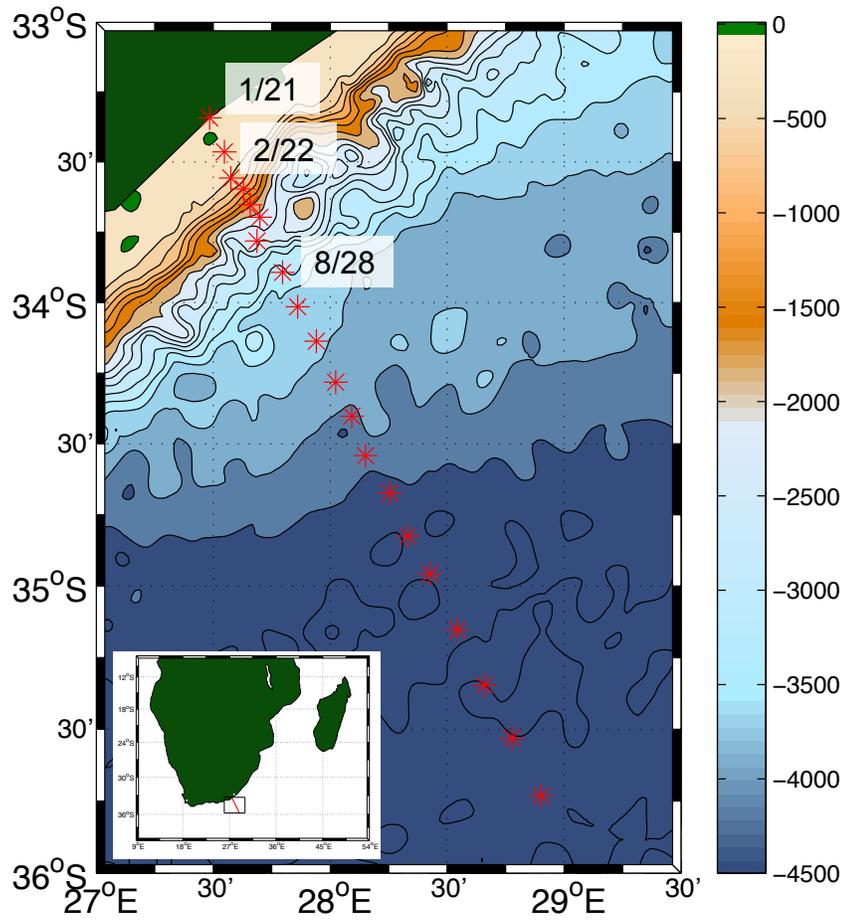
Figure 3.1: Location of hydrographic stations (red asterisks) off the coast of southeast South Africa. Inset map shows larger region. Bathymetry is shaded, with black contours every 250 m. Stations for each line are at the same geographic location, but are separated in time. Stations 1/21, 2/22 and 8/28, mentioned in the text, are labeled.
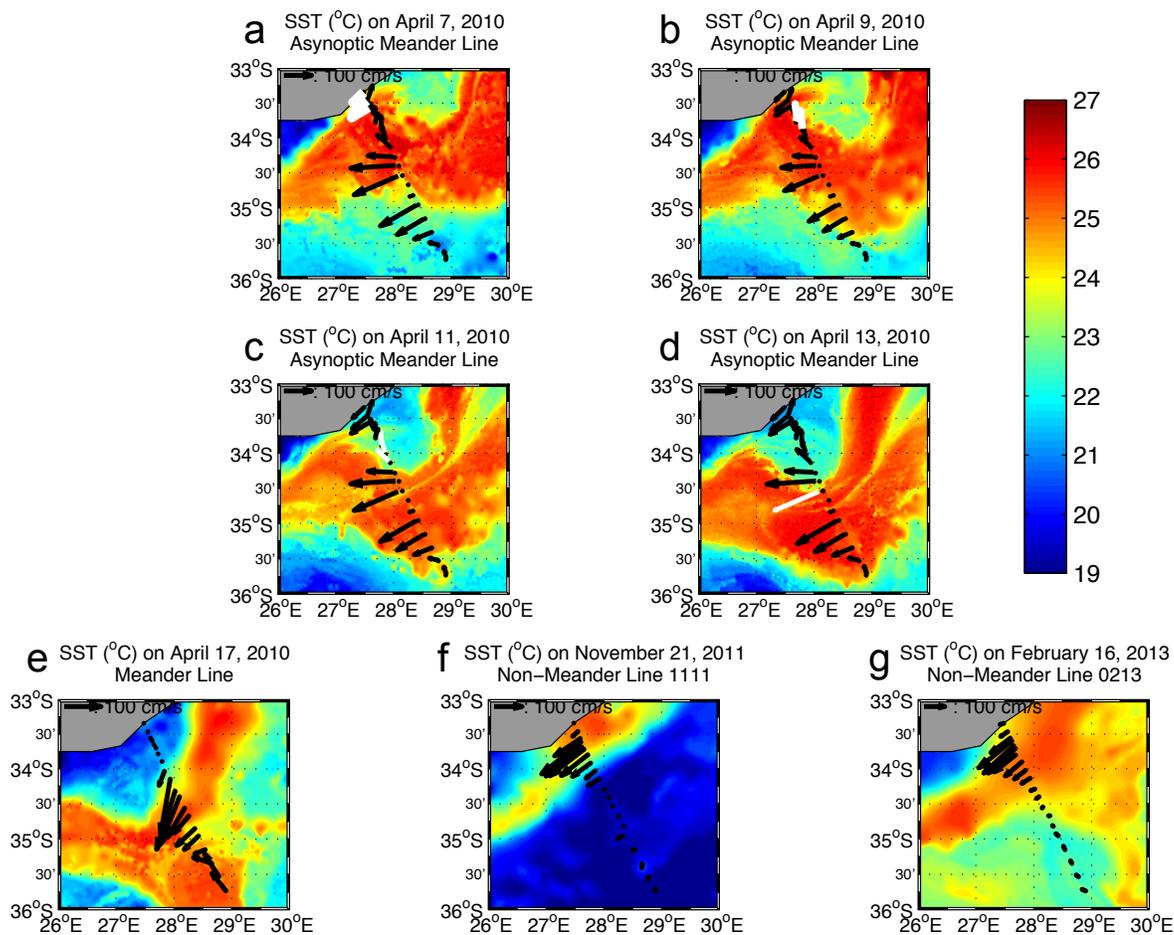
Figure 3.2: Maps of sea surface temperature (shading) and in situ velocity averaged over the upper 200m (black and white vectors) showing the meandering (panels a-e) and non-meandering (panels f-g) Agulhas Current. White velocity vectors show the portion of the LADCP data that was sampled at the same time as the underlying satellite data, given by the date above each panel, using the velocity scale given in the top left of each panel
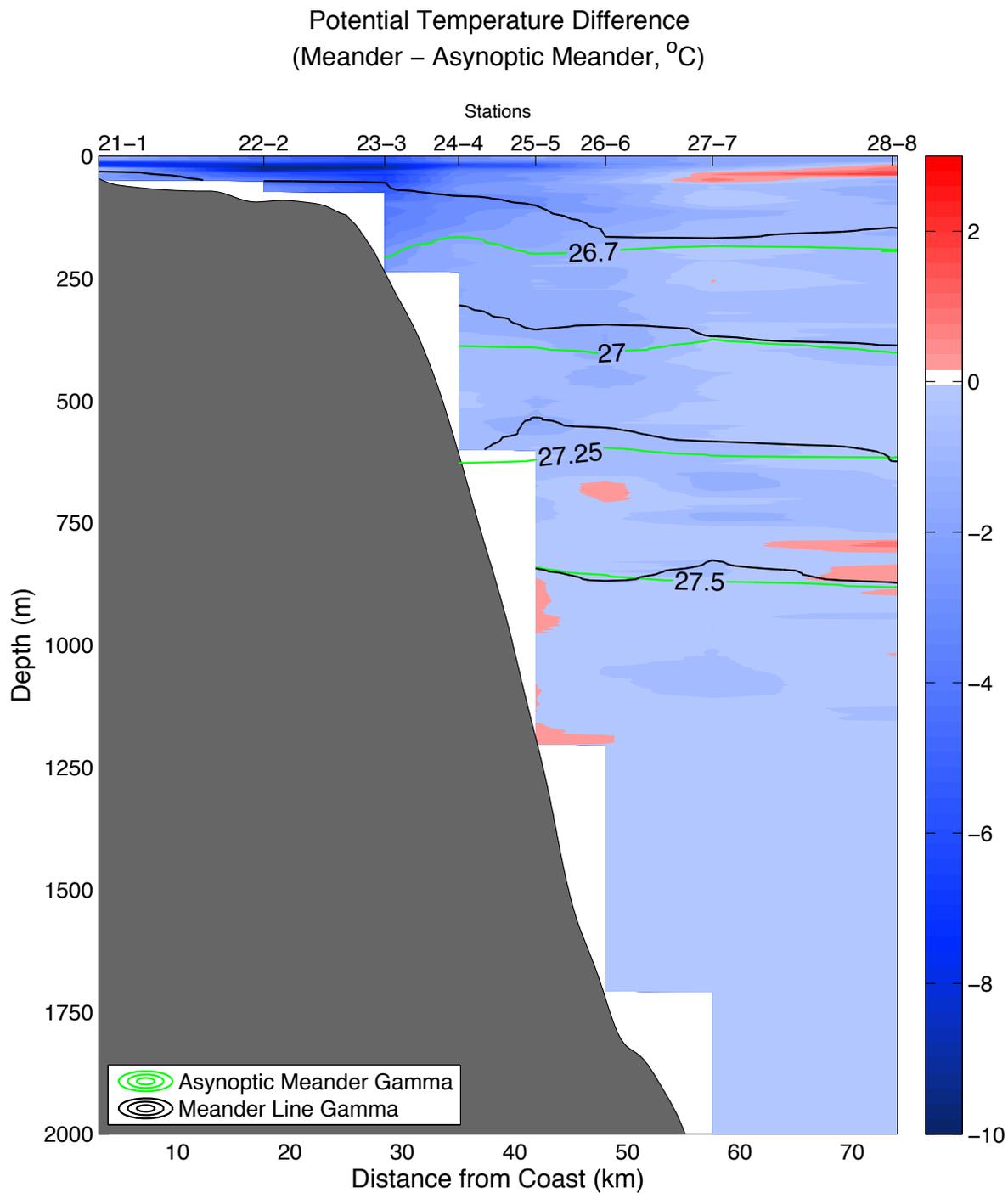
Figure 3.3: Potential temperature difference (°C) between the 8 inshore stations of the meander and asynoptic meander lines using the colorbar on the right. The overlain contours are neutral density isopycnals from the asynoptic meander line in green and meander line in black.
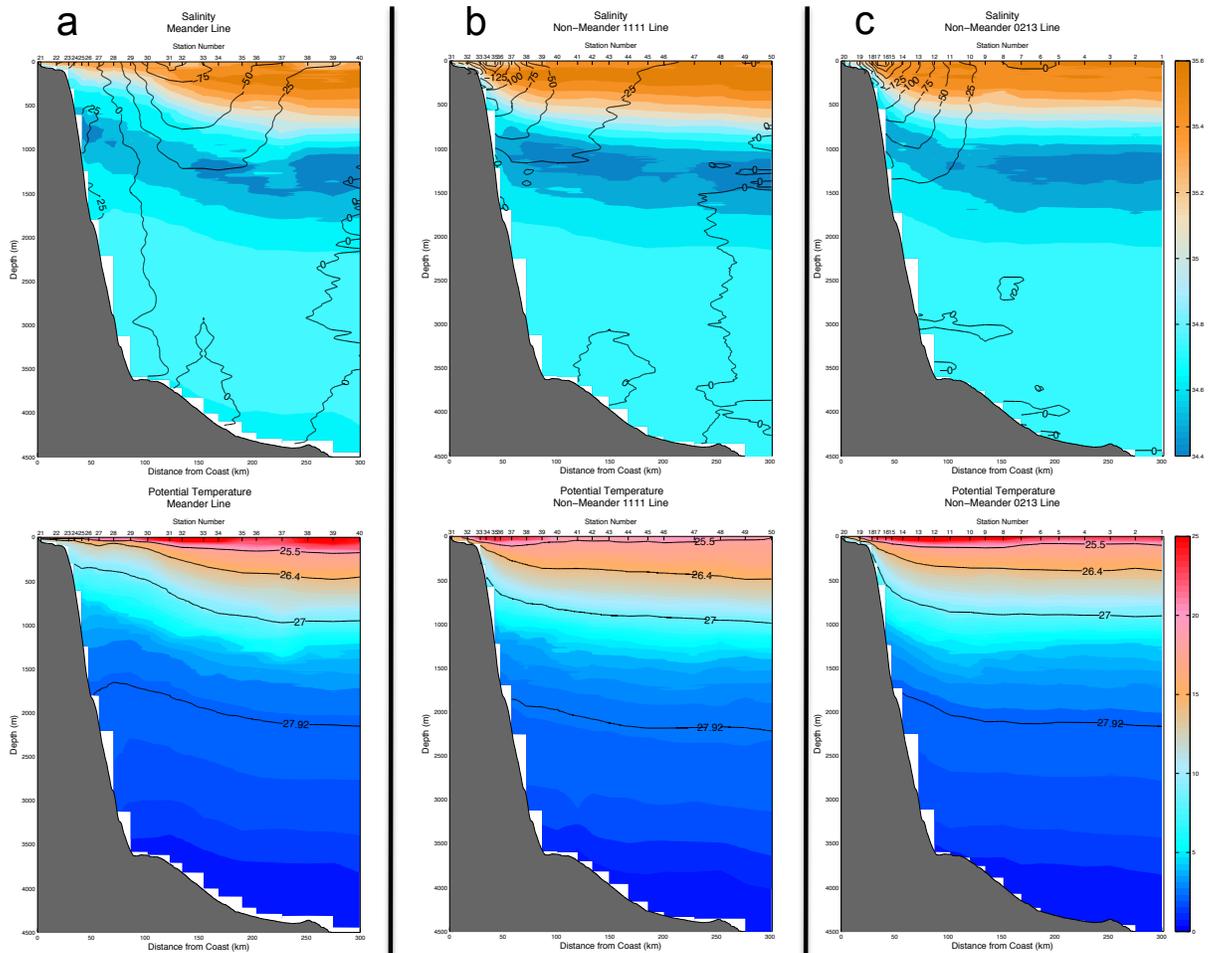
Figure 3.4: Cross-sections of salinity (top) and potential temperature (°C, bottom) for the meander line (a), non-meander 1111 line (b) and non-meander 0213 line using the colorbars to the right. Overlain contours show the LADCP velocity in 25 cm s^{-1} increments for the top panels and the 25.5, 26.4, 27 and 27.92 neutral density surfaces for the bottom panels.
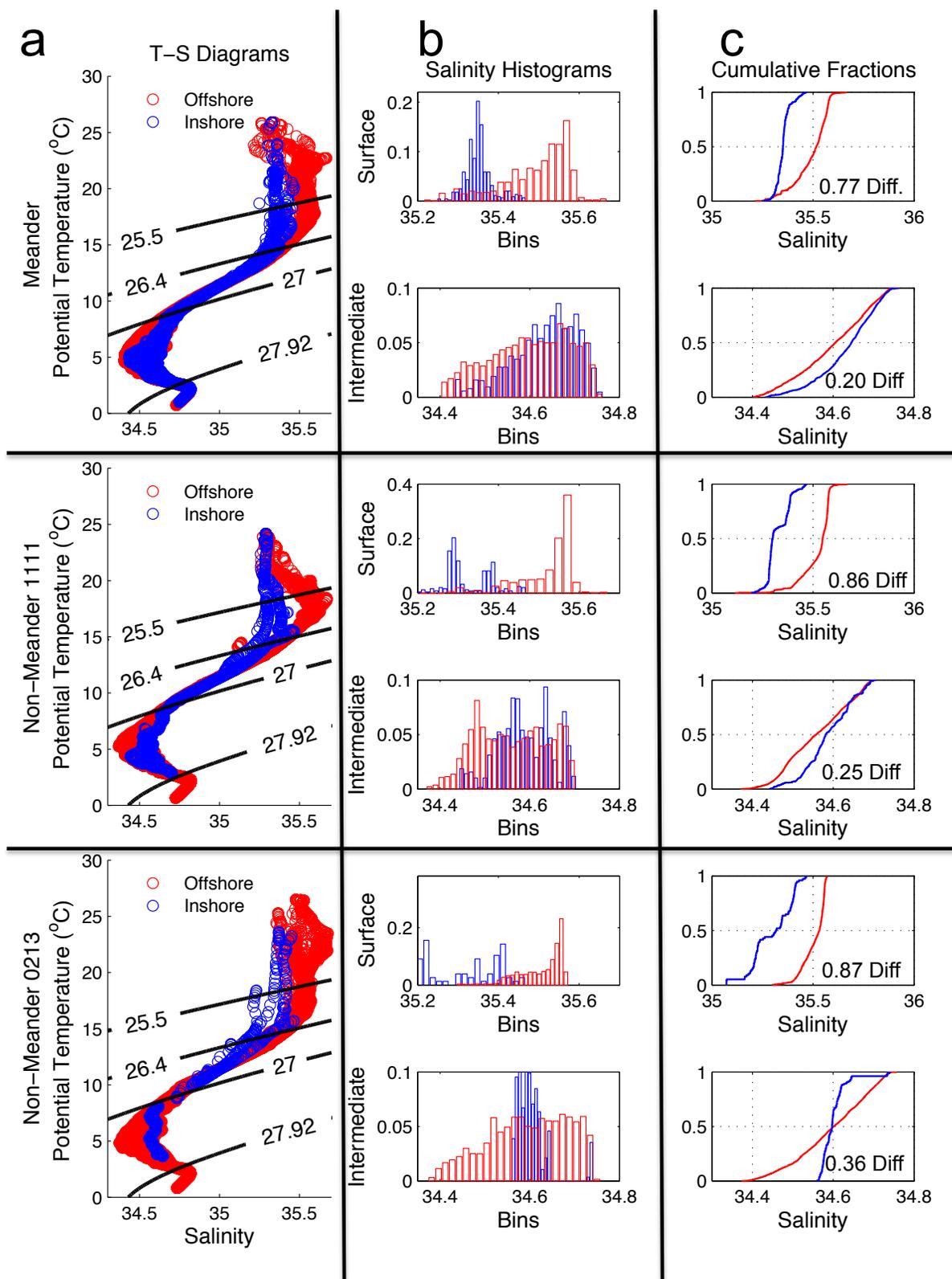
Figure 3.5: (Caption next page.)

Figure 3.5: (Previous Page) Potential temperature-salinity diagrams (a), salinity histograms (b) and salinity cumulative fraction plots (c) for the meander line (top), non-meander 1111 line (middle) and non-meander 0213 line (bottom). Surface data is defined as having a neutral density $\gamma < 26.4$, while intermediate data consists of neutral density values between $\gamma = 27.0$ and $\gamma = 27.92$, revealed by the neutral density contours overlaid in black on the left panels. Data with positive relative vorticity (offshore) are shown in red while data with negative relative vorticity (inshore) are shown in blue. Histogram and cumulative fraction plots alternate between surface and intermediate data, from top to bottom. Histograms have been normalized so that they represent the percentage of elements per bin rather than the total number of elements. The number in the bottom right of each cumulative fraction plot gives the maximum difference between distributions.
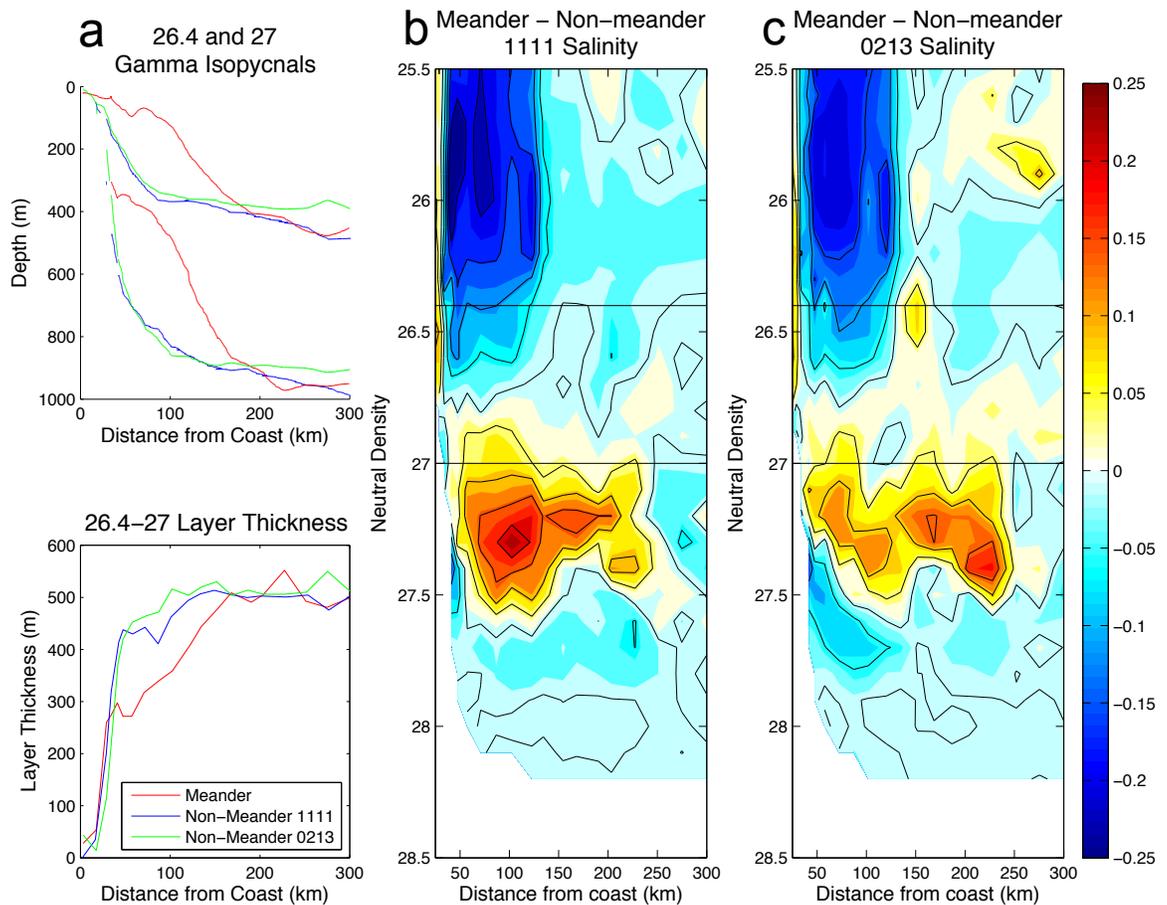
Figure 3.6: Neutral density layer $\gamma = 26.4$ - $\gamma = 27$ location (a, top) and thickness (a, bottom) for the meander (red), non-meander 1111 (blue) and non-meander 0213 (green) lines. Salinity difference (meander line minus non-meander 1111 line in b and meander line minus non-meander 0213 line in c) in neutral density space, using the color scale on the right. All fields are shown versus distance from coast.
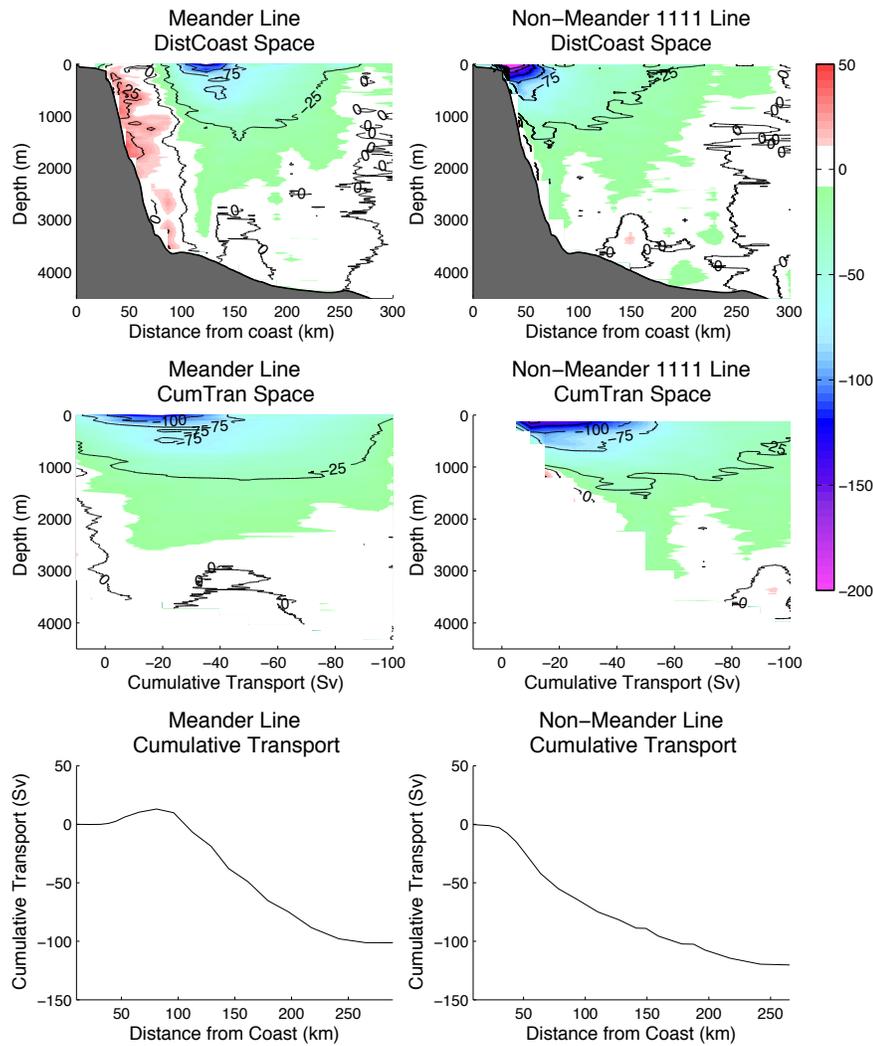
Figure 3.7: Six panels comparing the distance from coast coordinate system (top) with the cumulative transport streamline coordinate system (middle) for the meander (left) and non-meander 1111 lines (right). Colors are LADCP velocity normal to the hydrographic line defined as negative southwestward using the colorbar on the right. The overlain black contours show velocities in 25 cm s^{-1} increments from -100 cm s^{-1} to 25 cm s^{-1}. Bottom panels show the cumulative transport versus distance from the coast for the meander line (left) and non-meander line (right).
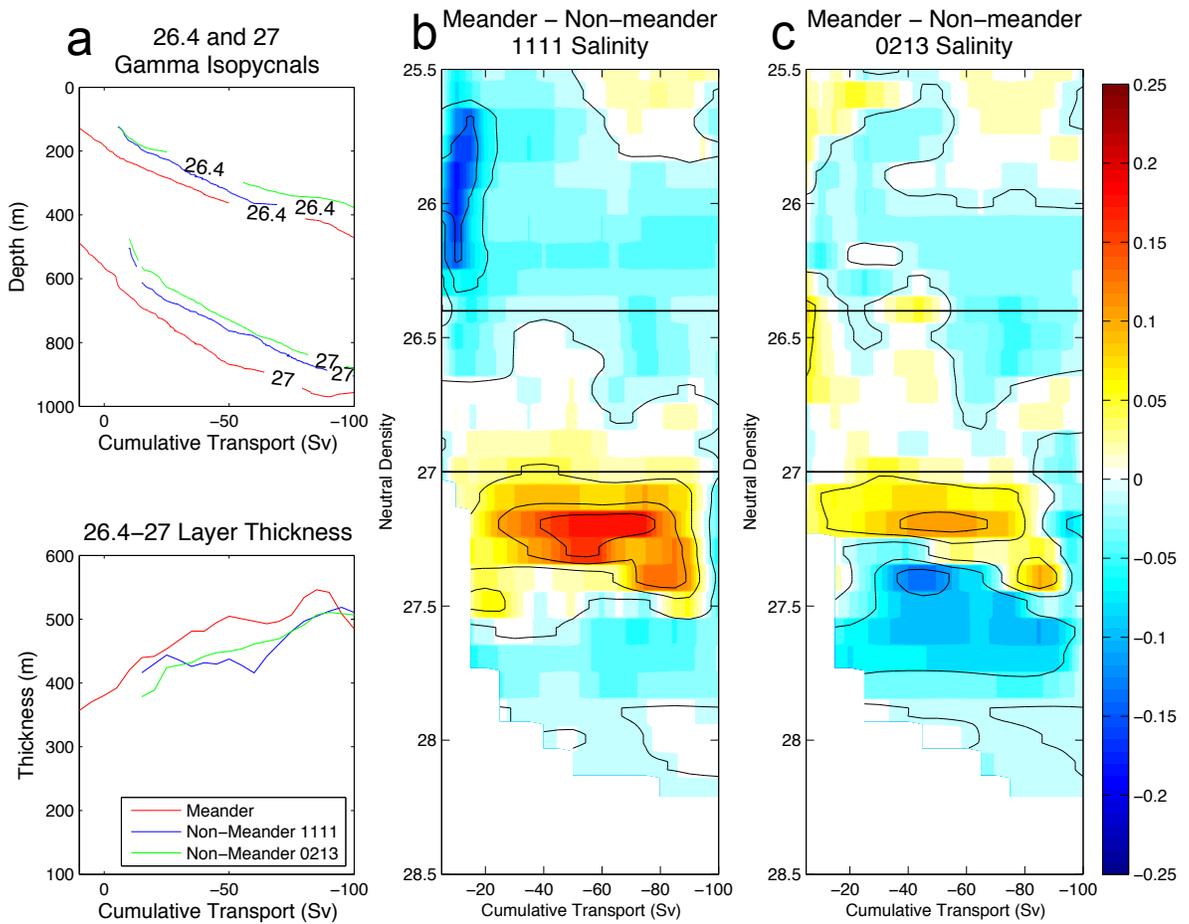
Figure 3.8: Same as in Figure 3.6, but for cumulative transport coordinates. Neutral density layer $\gamma = 26.4$ - $\gamma = 27$ location (a, top) and thickness (a, bottom) for the meander (red), non-meander 1111 (blue) and non-meander 0213 (green) lines. Salinity difference (meander line minus non-meander 1111 line in b and meander line minus non-meander 0213 line in c) in neutral density space, using the color scale on the right. All fields are shown versus cumulative transport as described in the text.
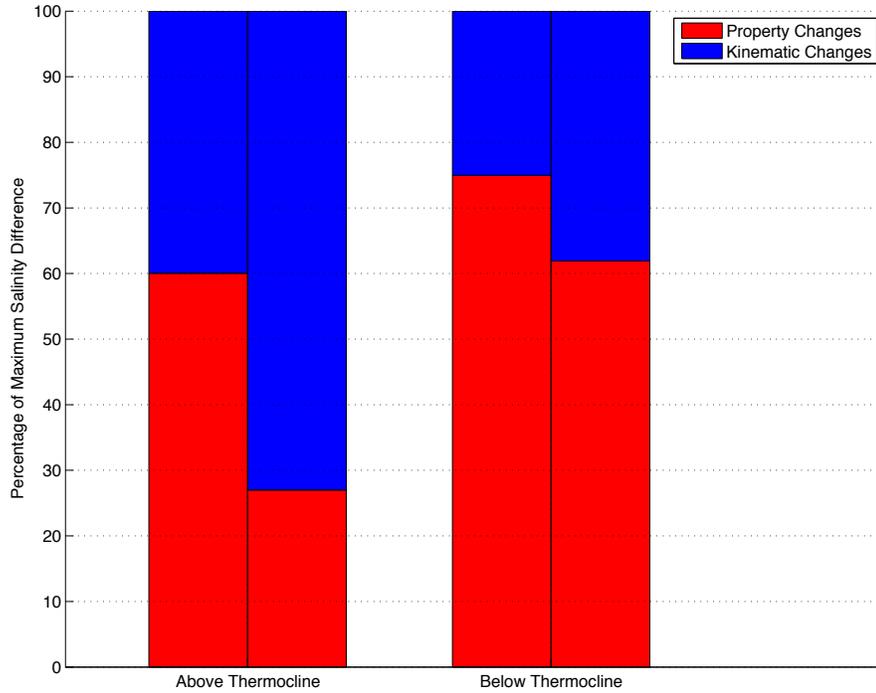
Figure 3.9: A bar graph showing the percent contribution of kinematic and property changes to the maximum change in salinity. Property changes are differences in the cumulative transport streamline coordinate system as described in the text. Kinematic changes are the residual between property changes and differences in the distance from coast coordinate system. The group of two bars on the left shows the breakdown in the near-surface layer above the thermocline, defined as between $\gamma = 25.5$ and $\gamma = 26.4$. The group of two bars on the right shows the breakdown below the thermocline, defined as $\gamma > 27$. Within each of these groups, the leftmost bar shows meander minus non-meander 1111 data and the rightmost bar shows meander minus non-meander 0213 data. Property changes are the portion of each bar in red and kinematic changes are the portion of each bar in blue.

Chapter 4

Current and Wind-driven Upwelling Events inshore of the Agulhas Current

In this chapter, we investigate upwelling events inshore of the Agulhas Current at approximately 34°S. These events exchange shelf and slope waters, potentially enhancing primary productivity along the shelf and advecting larvae and pollutants offshore. Hydrographic observations of a wind-driven upwelling event and a current-driven upwelling event show that they can advect slope waters more than 130 m upward onto the continental shelf resulting in a 9°C cooling. We use satellite data to extend these in situ data and assess the frequency, strength and forcing mechanisms of cold events during an 11-year period. We define cold events as days when the shelf-averaged sea surface temperature anomaly falls below the 95th percentile. We identify 47 events with an average length of 3.5 days and sea surface temperature anomaly of -2.4°C. We explore 4 forcing mechanisms: alongshore wind speed, wind stress curl, Agulhas Current core distance and Agulhas Current core speed. For all

forcing mechanisms, we find stronger forcing leads to longer cold events and, with the exception of Agulhas Current core distance, also colder events. Current-driven cold events occur 3 times more often than wind-driven cold events, but the latter are slightly stronger. 75% of cold events associated with strong wind stress curl are also associated with Agulhas meanders, suggesting that frontal curvature is driving local wind stress curl anomalies. The combination of these forcings leads to the strongest cold events. Cold event frequency exhibits strong seasonality, with most occurring in austral summer and fall. We believe this is due to the seasonality of the alongshore wind directionality, which is upwelling favorable from November to April.

4.1   Background

The Agulhas Current is the largest western boundary current in the Southern Hemisphere (Bryden et al., 2005), flowing southwestward along the African continent. Upwelling events in the Southern Agulhas Current are of particular interest since this region is home to several reproductive habitats including nursery and spawning areas (Hutchings et al., 2002). Upwelling promotes biological productivity as nutrient-rich water is advected from the adjacent (deep) ocean onto the shelf (Atkinson et al., 1983; Miller and Lee, 1995). When slope waters rise onto the shelf, they displace shelf waters offshore and facilitate the mixing of pollutants from coastal runoff and larvae offshore (Churchill et al., 1986; Porri et al., 2014). Upwelling events are especially important in western boundary current systems since the mean current acts as a strong barrier to mixing (Bower et al., 1985).

Inshore of western boundary currents, upwelling can be either current-driven or wind-driven. Observations show current-driven coastal upwelling is episodic, primarily fueled by eddies that develop when the current becomes unstable and meanders (Brandini, 1990; Castro and Miranda, 1998; Campos et al., 2000; Stabeno and

Van Meurs, 1999; Gawarkiewicz et al., 2001; Okkonen et al., 2003). Meanders induce upwelling along their trailing edge and downwelling along their leading edge, related to the dual passage of cyclonic and anticyclonic anomalies, which leads to confluent flows at the meander trough, and diffluent flows at its crest (Olson, 2002; Campos et al., 2000). Current-driven upwelling can also be caused by an increase in current speed, which intensifies Ekman transport in the bottom boundary layer facilitating upwelling along the continental shelf (Roughan and Middleton, 2002).

Alongshore winds or wind stress curl can also drive western boundary upwelling events. For the Agulhas Current region, northeasterly winds force offshore Ekman transport and coastal upwelling (Smith, 1995), while local, negative wind stress curl leads to surface divergence and upwelling.

Western boundary upwelling events have been studied previously within the Brazil Current system. Brandini (1990) discovered that nutrient concentrations along the shelf of the Brazil Current peak when meanders are present. Campos et al. (2000) showed that meanders bring intermediate South Atlantic Central Water (SACW) onto the continental shelf when alongshore winds are upwelling-favorable. Castelao et al. (2004) concluded that while solitary meanders brought SACW up to the shelf break, upwelling favorable winds were necessary to bring SACW onto the shelf. More recently, Castelao and Barth (2006) showed that the wind stress curl can be just as important a contributor to upwelling as alongshore winds. This phenomenon is not isolated to the Brazil Current as solitary meanders have also been shown to upwell intermediate waters within the Gulf Stream (Flierl and Davis, 1993; Lee et al., 1981).

Several studies have investigated upwelling events in the Southern Agulhas Current (Porri et al., 2014; Weidberg et al., 2015; Jackson et al., 2012) and show that meanders represent the strongest mode of temperature variability along the Agulhas Bank. These studies show that meanders drive cyclonic flow along the bank which

leads to temperature fluctuations and upwelling. Goschen et al. (2012) identified 55 upwelling events over a 7-month period at about 34°S, that caused cooling of between 2 and 10°C. Here, we present high-resolution hydrographic observations of both a current-driven and wind-driven upwelling event within the Agulhas Current at 34°S. We then expand our analysis to the time period 2003-2014 using satellite data to identify similar upwelling events. We assess the frequency of these large upwelling events as well as determine the relative importance of both current-driven and wind-driven forcing mechanisms.

4.2 Data and Methodology

4.2.1 Hydrographic Data

For this study, we use data from four separate hydrographic transects across the Agulhas Current close to 34°S collected during cruises in April 2010 and February 2013. Measurements were taken using a CTD (Conductivity, Temperature, Depth) and lowered acoustic Doppler current profilers (LADCP). The CTD package included a 12-bottle rosette and a Sea-Bird SBE9-11 with dual temperature, conductivity and oxygen sensors plus an altimeter. For the LADCP, a dual 300-kHz configuration was used during the April 2010 cruise, and a hybrid configuration (300 kHz upward-looking, 150 kHz downward-looking) was used during the February 2013 cruise.

During the April 2010 cruise, a large meander event was sampled. Meander line 1 was collected over five days of mooring operations from April 7-11 2010 (Figure 4.1c, stations 1-8). Meander line 2 was collected continuously on April 17 2010 (Figure 4.1c, stations 21-28). During the February 2013 cruise, an upwelling-favorable wind event was sampled. Wind line 1 was collected over 2 days from 17-18 February 2013 (Figure 4.2c, stations 20-13). Wind line 2 was collected over 2 days from 25-26 February

2013 (Figure 4.2d, stations 34-41). For our analysis, we focus on the continental shelf region, limiting our analysis to the top 500 m and within 75 km of the coast.

4.2.2 Satellite Data

To define cold events, we employ daily, 1.5-km resolution, gridded sea surface temperature (SST) data from the group for high resolution SST (GHRSST). Xie et al. (2008) show that this product has large coastal biases in water shallower than 40 m. Hence, we define cold events using area-averaged SST over a region that extends from the coast out to the 2500-m isobath (Figure 4.1a). Making the box smaller does not significantly alter the results presented here.

In order to separate cold events from seasonal and longer timescale variability, we first subtract an annual cycle, defined as the mean temperature from each day over all years. Our resulting seasonal cycle ranges from 19.4 °C in mid-August to 24.6 °C in late February (Figure 4.3). We then apply a 13-month high pass filter to get SST anomalies (SSTA). We define cold events as days with SSTA less than 1.96 standard deviations below the mean for our time record, or below -1.8°C. This threshold was chosen for three reasons. First, it incorporates the SSTA values for both of our observed cold events. Secondly, assuming that our data is normally distributed, it represents the coldest 2.5% of our dataset. Last and most important, it represents a threshold at which cold events significantly correlate with wind and current forcing mechanisms. This gives us confidence that we are capturing local upwelling, rather than alongshore advection. Our method identifies less events than Goschen et al. (2012), whose in-situ data detected cold events of smaller magnitude, but which may not directly relate to wind or current forcing.

We can assess local forcing mechanisms using satellite altimetry and wind data. We use along-track absolute dynamic topography (ADT) from Archiving, Validation

and Interpretation of Satellite Oceanographic Data (AVISO). The AVISO ADT product is computed as a mean sea surface from along-track mean profiles (based on Rio et al. (2011)), plus a sea level anomaly minus a geoid (calculated from hydrographic data and 4.5 years of Gravity Recovery And Climate Experiment data from 1993-1999). The along-track data is provided every 10 days with a horizontal resolution of $\frac{1}{4}^\circ$. We use the ADT to define two separate current-driven forcing mechanisms: meandering and increased current strength. Meanders can be related to the offshore distance of the Agulhas current core, which we find as the location of the maximum ADT gradient, ACDist. Since we are interested in anomalies, we remove seasonal variability from all forcing mechanisms. In the case of the ACDist variable, we find that the seasonal cycle is insignificant. Meanders are defined as times when ACDist is one standard deviation above the time-mean, or greater than 85 km offshore.

Current strength is also calculated using the maximum ADT gradient, such that:

$$Geovel = \frac{f}{g} max(\frac{\partial h}{\partial x}) \qquad (4.1)$$

where Geovel is the maximum southwestward cross-track geostrophic velocity, f is the Coriolis force, g is gravity, h is ADT, and x is the along-track direction, positive to the southeast. We subtract an annual cycle from Geovel, which is a minimum in austral summer and maximum in austral spring (Figure 4.3), in agreement with Krug and Tournadre (2012). We expect strong Geovel to influence upwelling through increased shoreward Ekman transport in the bottom boundary layer. We define Geovel events as one standard deviation below the time-mean ($<$-0.40 m s^{-1}). Both current-driven forcing mechanisms, Geovel and ACDist, are interpolated linearly to daily values.

Wind-driven forcing mechanisms are calculated using Cross-Calibrated Multi-Platform (CCMP) ocean surface winds (Atlas et al., 2011). CCMP winds use a

variational analysis method on combined cross-calibrated satellite winds to produce a global $\frac{1}{4}$ degree, 6-hourly u,v wind product. The variational analysis method combines data from several remote sensing systems and in situ measurements with a first guess of the wind field (Hoffman et al., 2003). CCMP winds are validated against moored ocean buoys to which they agree within 0.8 m s^{-1}. We first subtract the seasonal cycle from both the u and v wind data. Alongshore winds are upwelling-favorable from November to April (Figure 4.3). Removing the seasonal cycle does not significantly alter wind stress curl, which has weak seasonality (Figure 4.3). We use these deseasoned wind data to find upwelling-favorable anomalies in alongshore wind and wind stress curl. We rotate winds to alongshore and define strong Ashorewnd as times when alongshore winds are one standard deviation below the time-mean ($<$-6.6 m s^{-1}). Wind stress curl is determined using the Large and Pond (1981) wind stress formulation. We define upwelling-favorable curl events as times when wind stress curl is one standard deviation below the time-mean ($<$-1.6E-2 N m^{-3}). For basic statistics on SSTA as well as our four defined forcing mechanism anomalies, see Table 4.1.

4.3 Results

4.3.1 Hydrographic Observations of Upwelling Events

4.3.1.1 Meander-Induced Upwelling

Meander line 1 (Figure 4.1a and 4.1c) captured the Agulhas Current just prior to separation, while meander line 2 (Figure 4.1b and 4.1d) was occupied during the fully-developed meander. Comparison between these two times show that the meander causes a 4.5 °C drop in SST and 9 °C drop in potential temperature at mid-depth (50 m) along the mid-shelf region (Figure 4.1). These temperature changes coincide with an uplift of the neutral density surface γ=26.7 (Jackett and McDougall, 1997),

or upwelling of South Indian Central Water (SICW) (Beal et al., 2006). Satellite data confirms that this cold event was current-driven, and that it drives a local wind stress curl anomaly after it has fully developed.

For a more thorough description of this meander event and its associated isopycnal and diapycnal fluxes, see Leber and Beal (2014) and Leber and Beal (2015). The area-averaged inshore SSTA on 9 April 2010 is 1.2 °C. This value falls to -2.5 °C on 16 April 2010 and stays below our anomaly threshold through 22 April 2010 for a cold event length of 7 days. The offshore distance of the AC core passes our threshold value of 85 km on 10 April 2010 and remains anomalous until 25 April 2010, although the inshore SSTA is below the threshold only until 22 April 2010. During this cold event, neither Agulhas Current core strength nor alongshore winds surpass their threshold values. Wind stress curl surpasses its threshold on 22-23 April 2010. This suggests that the frontal curvature of the meander forces a local wind stress curl that acts to enhance upwelling. This idea will be explored further in Section 3b,2.

4.3.1.2 Wind-Induced Upwelling

In February 2013, we observed an upwelling event driven by strong northeasterly winds. Comparison between wind lines 1 and 2 show a 4 °C drop in SST within our boxed region (Figure 4.2). Unlike the meander-driven upwelling of April 2010, the Agulhas Current maintains its position along the shelf break during this time. Shipboard wind data reveals a strengthening of the upwelling-favorable northeasterly winds on 17 February 2013. The structure of cooling along the shelf is very similar to that seen in the meander-driven upwelling event with a 9°C cooling over the shelf and a 189 m uplift of the $\gamma = 26.7$ neutral density layer or SICW. The lack of strengthening or offshore movement of the current during this time confirm that this event was entirely wind-driven, with little to no contribution from current-driven forcing mechanisms.

During this event, inshore SSTA within the boxed region is below its threshold for only one day (17 February 2013, -2.42 °C), during which upwelling-favorable alongshore winds averaged -11 m s^{-1}. 8 days later, the upwelling event is over and alongshore shipboard winds have weakened to -5 m s^{-1} (Figure 4.2b and 4.2d). For this particular event we use shipboard wind data since CCMP wind data is unavailable. Isopycnal uplift is dramatic during this cold event. SICW, illustrated by the γ=26.7 neutral density contour, intrudes over the shelf and up to 15 m depth while alongshore winds are strong, compared to its more typical depth of 200 m observed 8 days later (Figure 4.2c and Figure 4.2d). At the same time, the Agulhas Current core has neither moved nor strengthened significantly. Therefore, this cold event can be attributed entirely to the strong negative alongshore winds rather than any current-driven forcing mechanisms.

It is worth highlighting that both the wind-induced and current-induced events cause the same magnitude temperature change and neutral density uplift despite the different forcing mechanism and timescale of the event. Next, we use satellite data to expand our analysis to the 11 year period spanning 2003 through 2014.

4.3.2 Satellite Observations of Cold Events

4.3.2.1 Cold Event Classification and Characteristics

We define cold events as times when the area-averaged SSTA falls below the 95th percentile (<-1.8 °C). If we use SSTA thresholds that allow for weaker cold events, correlations with local forcing become insignificant. For the time period between 2003 and 2014, we find 166 days of cold events, representing 47 individual events with an average length and standard deviation of 3.5 ± 3.4 days (Figure 4.4). This is just over 4 events on average per year.

Although upwelling events are normally considered important for their ability to promote biological productivity, we must note that the average length of our identified events is unlikely to promote sustained biological productivity (McClain and Atkinson, 1985). Hence, the major importance of these short-lived upwelling events is likely related to their ability to advect surface waters offshore, which can create larval population sinks (Porri et al., 2014).

The distribution of SSTA is skewed towards cold events, with a range from -4.1 °C to 2.6 °C. Cold anomalies are more rare, but stronger than warm anomalies, and they represent 4% of our timeseries, exceeding the 2.5% that would be expected from a normal (Gaussian) distribution.

Cold events range in length from 1 to 14 days. The correlation between length and maximum strength (minimum SSTA) is -0.74, which is significant at the 99% level. Hence, longer events are colder.

4.3.2.2   Cold Event Forcing Mechanisms

All four forcing mechanisms are significantly correlated with the length and maximum strength of cold events (Figure 4.5), with the exception of current meandering which significantly influences the length but not the strength of cold events. Stronger upwelling favorable winds, wind stress curl and current strength all lead to longer and stronger events, as expected.

Our hydrographic data shows that our cold events are associated with a temperature drop of close to 9°C, which suggests that only large events are correlated to local forcing. We believe this is why we identify far fewer upwelling events than Goschen et al. (2012). Over a seven month period, they identify 55 upwelling events at a site close to ours. Many of these events are associated with a 2-5 °C cooling, and the authors attribute a large number of them to remote forcing by coastal-trapped waves.

Goschen et al. (2012) identify 3 events with a 9°C temperature change, consistent with our finding of 4 large upwelling events per year.

Surprisingly, there does not appear to be a strong relationship between the type of forcing mechanism and the average length or strength of an event. Our in-situ data suggests that current-driven cold events are longer than wind-driven cold events, however over eleven years of events this is not the general case.

There is a strong seasonality of cold events, which peak from austral summer to fall (Figure 4.6). This seasonality is tied to the seasonal cycle of alongshore winds, which are upwelling-favorable from November through April. Hence, cold events are more likely to occur during the time that the background seasonal cycle of alongshore winds enhances upwelling. Castelao et al. (2004) identified a similar seasonality in the Brazil Current: although meanders initiated upwelling, upwelling-favorable winds were necessary for the upwelling to reach the continental shelf.

We find that the four forcing mechanisms are not independent. There are significant correlations between both curl and meandering as well as between alongshore wind and wind stress curl (Table 4.2). The correlations between all other forcing mechanisms are statistically insignificant.

The -0.25 correlation between meandering and curl, significant at the 95% level, suggests that upwelling favorable wind stress curl patterns tend to coincide with meander events. In fact, of the 8 cold events during a strong curl, 6 occur during meanders (Figure 4.5e). The average SSTA during these 6 events is -2.6 °C, which is stronger than for any other one forcing mechanism alone. This relationship between wind stress curl and meandering may be evidence of frontal systems influencing local wind stress patterns as has been observed in the western Arabian Sea (Vecchi et al., 2004). To investigate this feedback, we follow Chelton et al. (2007) and consider the correlation between the crosswind SST gradient and the wind stress curl. We

find a highly significant correlation of 0.57 for the entire timeseries. This correlation strengthens slightly to 0.61 when we consider the correlation during cold events. Hence, the migration of the Agulhas Current front drives local wind stress curl, such that upwelling resulting from a meander event is enhanced further.

We also find a significant anticorrelation between alongshore wind and wind stress curl (Table 4.2), which suggests that the two wind-driven forcing mechanisms tend to oppose each other in terms of promoting upwelling. Figure 4.7b shows that cold events during times of strong wind stress curl are also associated with strong positive alongshore winds. The average alongshore wind during cold events with strong wind stress curl is 10.8 m s^{-1}, which is strongly downwelling favorable (Table 4.3). Cold events during times of strong negative alongshore wind coincide with times of strong positive wind stress curl (2E-2 N m^{-3}, Table 4.3, Figure 4.7e). Since wind strength decreases offshore, upwelling-favorable (downwelling-favorable) alongshore winds necessarily create downwelling-favorable (upwelling-favorable) wind stress curl patterns.

It may appear surprising that the correlation between alongshore wind and current strength is insignificant (Table 4.2). A strong negative alongshore wind drives offshore transport that could strengthen the pressure gradient across the current and lead to increased geostrophic velocity (Lee and Williams, 1988). The lack of significant correlation between our alongshore winds and current strength is simply due to the fact that we have removed the seasonal cycle of each of these variables. In fact, the correlation between the seasonality of current strength and alongshore winds is 0.75, which is 99% significant (Figure 4.3). This signal is removed for our data since we are interested in short-term anomalous events.

The dependencies among forcing mechanisms are highlighted by composites showing the structure of each type of cold event and its forcing (Figure 4.7). Cold events

forced by wind stress curl and meandering appear similar since most curl events occur during meanders (Figure 4.7a,b). In fact, the average Agulhas Current offshore distance during wind stress curl events is 105 km (Table 4.3). The wind patterns during wind stress curl forcing and alongshore wind forcing confirm their strong anticorrelation (Figure 4.7b,e). Compared to the time-mean (Figure 4.7c), average cold events are associated with a greater Agulhas Current core distance and strength (Figure 4.7f). The time-mean Agulhas Current core distance is 60, but averages 91 km during cold events (Table 4.3). During the average cold event, winds are not upwelling-favorable and are, in fact, onshore with positive inshore wind stress curl (Table 4.3, Figure 4.7). These patterns are a result of the greater frequency of current-driven forcing mechanisms compared to wind-driven forcing mechanisms.

Of the identified cold event days, 66% occur during times of strong current-driven forcing and 23% occur during times of strong wind-driven forcing (Table 4.3). Approximately half of all cold event days occur during meanders and 33% during increased current strength. Both meanders and increased current strength occur for 14% of cold event days. Strong wind stress curl influences just 5% of cold event days, but is also dependent on meandering and downwelling winds and does not appear to be an independent forcing mechanism. Alongshore winds act independently to influence 18% of cold event days. Any one or more of these four local forcing mechanisms is strong sometime during 81% of cold event days and 93% of cold events. It is interesting to note that this last value is not 100%, as has been seen in the Brazil Current region (Aguiar et al., 2014). This suggests that the Agulhas Current is a more complex system with some cold events due to remote forcing, such as coastal-trapped waves or advection (Goschen et al., 2012).

4.4 Summary

Upwelling events inshore of the Agulhas Current at 34°S are forced by both wind and current mechanisms. Hydrographic data show that both Agulhas Current meander events and strong northeasterly winds can lead to upwelling that cools the mid-shelf region by 9°C. This cooling coincides with an uplift of South Indian Central Water as much as 190 m onto the continental shelf. This is similar to the current and wind-driven upwelling events of the Brazil Current that bring South Atlantic Central Water onto the shelf (Campos et al., 2000). The observed meander event lasts 7 days and drives upwelling-favorable wind stress curl. The single day wind event is forced by northeasterly winds alone, with no influence from upwelling-favorable current effects.

We study cold events between 2003 and 2014 that are significantly correlated with upwelling forcing mechanisms. We consider alongshore wind speed, wind stress curl, Agulhas Current strength and offshore distance. Over the 11 year period, we identify 47 individual cold events with an average length of 3.5 days. Our in-situ data shows that these events are able to advect intermediate, high-nutrient, waters on to the continental shelf, but their short timescale suggests they likely do not promote biological productivity. Observations show that western boundary current upwelling does not enter the euphotic zone due to its deeper extent (Chavez and Toggweiler, 1994), so that the major importance of upwelling events such as these are likely related to offshore advection of surface waters that contain larvae (Porri et al., 2014). Although our in-situ data suggest otherwise, neither the length nor strength of cold events are associated with the type of forcing mechanism. Most cold events occur in austral summer and fall, because prevailing winds are upwelling-favorable between November and April.

Wind stress curl anomalies are associated with meanders, such that 75% of strong wind stress curl cold event days coincide with meanders. A highly significant corre-

lation between the crosswind SST gradient and the local wind stress curl confirms that frontal variability is forcing local wind stress curl. Cold events where both the Agulhas Current core distance and wind stress curl are anomalous are the coldest. Wind stress curl is also highly anticorrelated with alongshore wind. This is due to the general pattern of wind speed decreasing with offshore distance. Upwelling-favorable alongshore winds set up downwelling-favorable wind stress curl and vice versa.

Roughly 3 times as many cold events are current-driven as wind-driven so that the structure of the average cold event has upwelling-favorable current anomalies but neutral/downwelling-favorable winds. Half of all cold events are associated with meanders, while roughly one quarter are associated with increased current strength. Alongshore winds are found to be an important forcing mechanism for 18% of events and wind stress curl is important for just 5% of events. At least one of these forcing mechanisms explains 81% of the observed cold event days.

	Minimum	Maximum	Mean	Standard Deviation	Threshold	Correlation with SSTA
ACDist (km)	22.5	207.2	60.4	24.8	85.1	-0.28
Geovel (ms^{-1})	-2.14	1.28	0.00	0.41	-0.4	0.18
Curl (Nm^{-3})	-1.3E-01	9.9E-02	3.5E-03	1.9E-02	-1.6E-02	-0.004
Ashorewnd (ms^{-1})	-17.0	23.2	0.3	6.9	-6.6	0.03
SSTA (°C)	-4.1	2.6	0.0	0.9	-1.8	1.00

Table 4.1: Table showing some of the basic statistics for the four identified forcing mechanisms: ACDist, Geovel, Curl and Ashorewnd (as defined in the text). For each of these forcing mechanisms as well as for SSTA, we provide (from left to right) the minimum, maximum, mean, standard deviation, threshold and correlation with SSTA.

	ACDist	Geovel	Curl	Ashorewnd
ACDist		-0.14	-0.25*	0.10
Geovel			0.06	-0.15
Curl				-0.47*
Ashorewnd				

Table 4.2: Correlation matrix for the four forcing mechanisms (as defined in the text): ACDist, Geovel, Curl, and Ashorewnd. Correlations marked with an asterisk are significant at the 95% level.

	ACDist > 85 km	Geovel < -0.40 ms^{-1}	Curl < -0.016 Nm^{-3}	Ashorewnd < -6.6 ms^{-1}	Cold Event Average	Timeseries Average
ACDist (km)	113	93	105	86	91	60
Geovel (ms^{-1})	-0.21	-0.7	-0.17	-0.19	-0.3	3.2E-03
Curl (Nm^{-3})	3.0E-03	1.4E-03	-4.5E-02	2.0E-02	4.3E-03	1.0E-03
Ashorewnd (ms^{-1})	0.3	0.6	10.8	-8.7	-0.2	0.3
SSTA (°C)	-2.3	-2.4	-2.5	-2.4	-2.4	0.0
Number of days	78	55	8	30	166	3996

Table 4.3: Table showing average values of ACDist, Geovel, Curl, Ashorewnd and inshore SSTA. These values are shown during periods of ACDist above 85 km, Curl below -0.016 N/m^3, Geovel below -0.40 m/s, Ashorewnd less than -6.6 m/s as well as the average during cold events and for the entire timeseries.
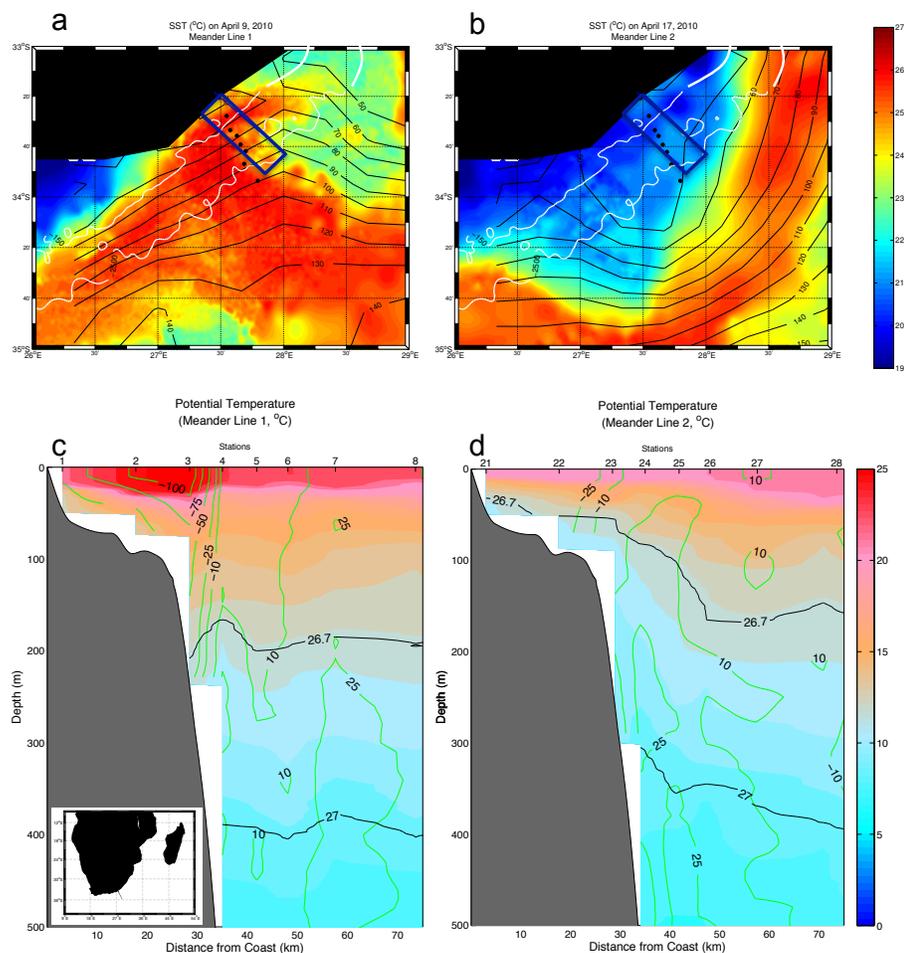
Figure 4.1: Top panels show satellite data for the April 2010 meander-induced cooling event. Colors show GHRSST SST using the colorbar on the right for April 9, 2010 (a) and April 17, 2010 (b). The overlain white contours show the 150 m and 2500 m isobaths. The overlain black contours show AVISO MADT in 10 cm increments from 50 to 150. The dark blue box encloses the region we've defined in the text as the inshore region for area-averaging. The black dots show the locations of the 8 hydrographic stations. Note that hydrographic stations are at the same geographic location but are separated in time. Bottom panels show our hydrographic observations of the meander-induced cooling event (c and d). Colors show potential temperature for the first 75 km and top 500 m for the first (c) and second (d) meander lines using the colorbar on the right. Green overlain contours represent cross-track LADCP velocity in 25 cm/s increments. Black contours represent the 26.7 and 27 neutral density surfaces for each line. The embedded figure in the bottom left of panel c gives the geographic context for this data, found at approximately 34°S off the southeast coast of South Africa.
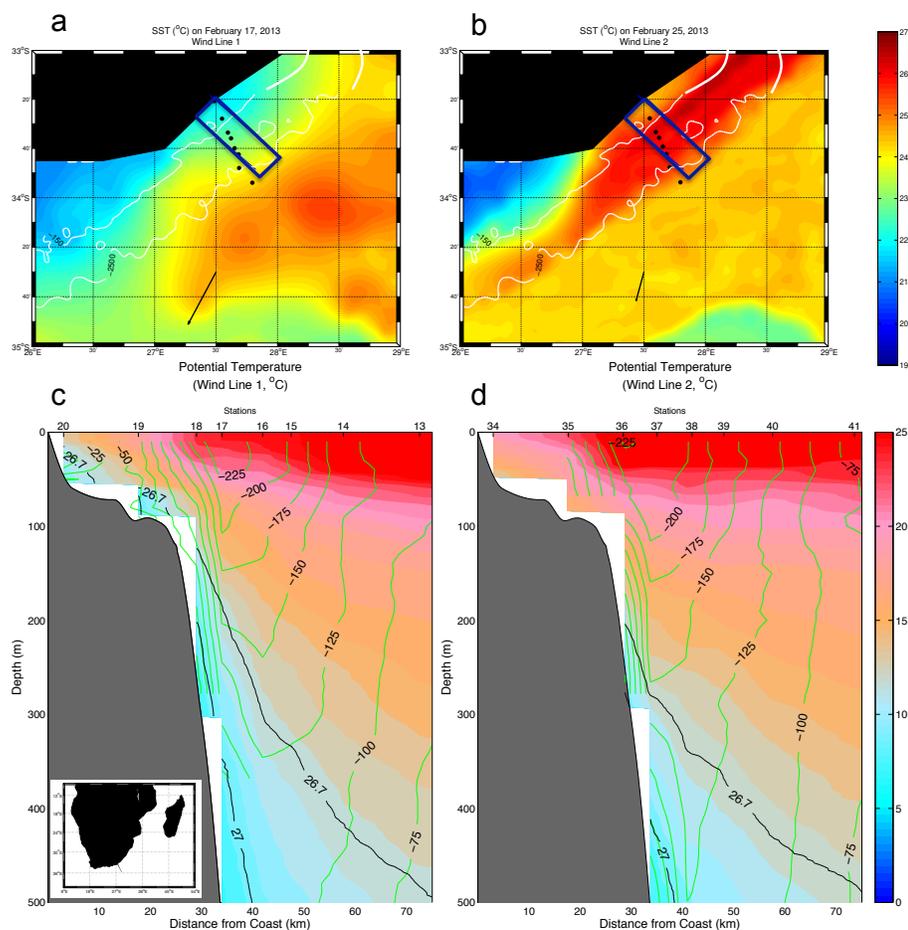
Figure 4.2: Same as Figure 4.1 but for the February 2013 wind-induced cooling event. Colors show GHRSST SST using the colorbar on the right for February 17, 2013 (a) and February 25, 2013 (b). The overlain white contours show the 150 m and 2500 m isobaths. We exclude the contours of AVISO MADT and instead include a vector at 34.5 °S and 27.5 ° E showing the average winds from the shipboard data for February 17, 2013 (a) and February 25, 2013 (b). The dark blue box encloses the region we've defined in the text as the inshore region for area-averaging. The black dots show the locations of the 8 hydrographic stations. Note that hydrographic stations are at the same geographic location but are separated in time. Bottom panels show our hydrographic observations of the wind-induced cooling event (c and d). Colors show potential temperature for the first 75 km and top 500 m for the first (c) and second (d) wind lines using the colorbar on the right. Green overlain contours represent cross-track LADCP velocity in 25 cm/s increments. Black contours represent the 26.7 and 27 neutral density surfaces for each line. The embedded figure in the bottom left of panel c gives the geographic context for this data, found at approximately 34°S off the southeast coast of South Africa.
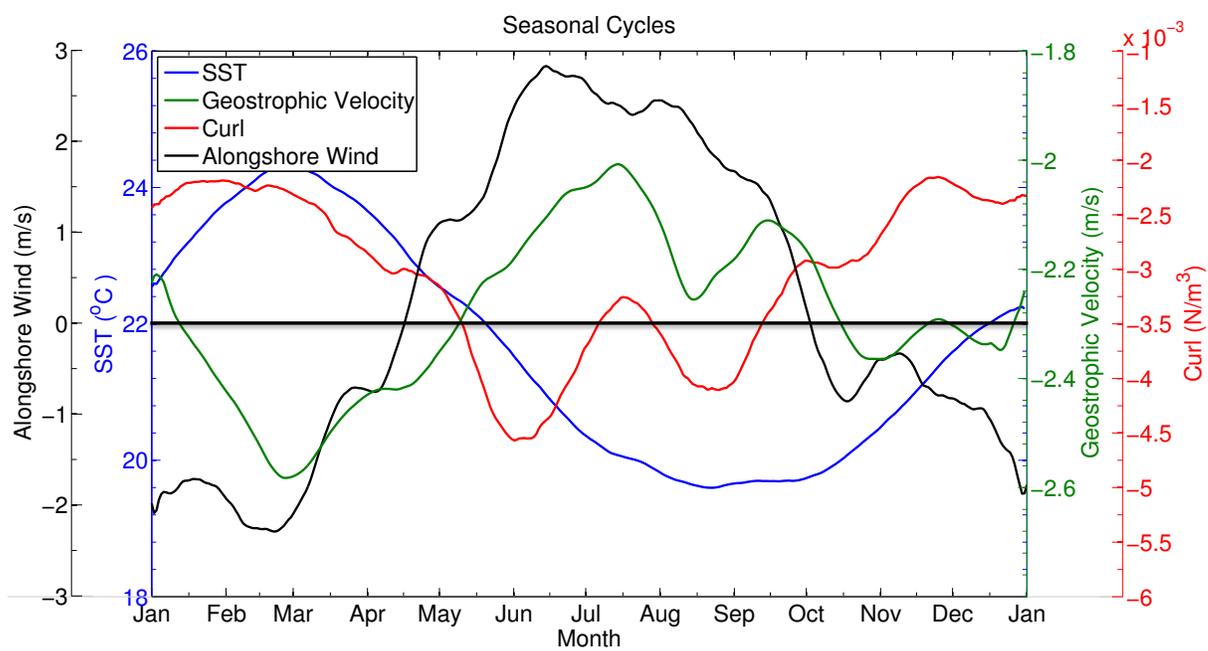
Figure 4.3: Seasonal cycles of SST (blue), Geostrophic velocity (green), curl (red) and alongshore winds (black).
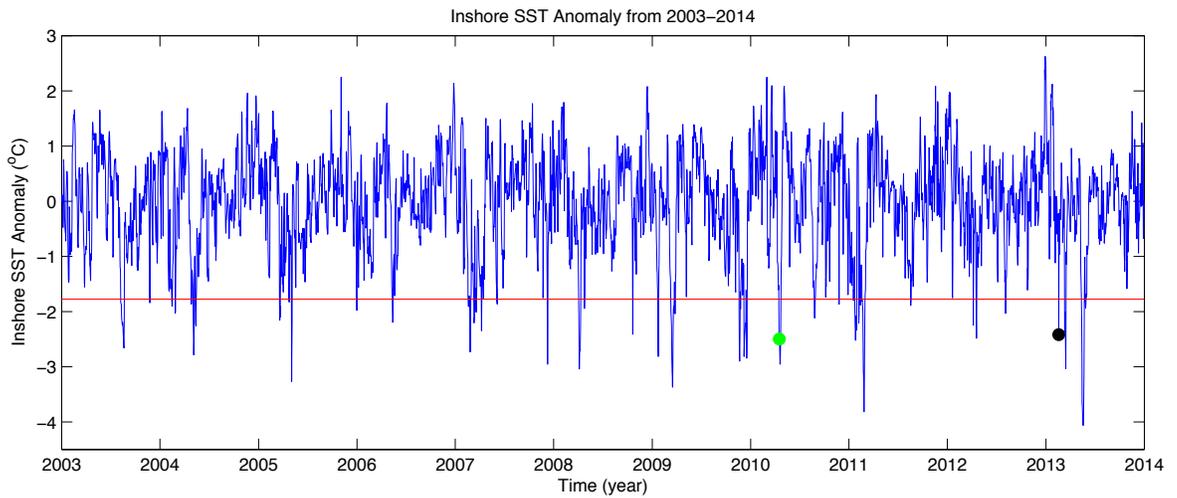
Figure 4.4: Inshore sea surface temperature anomaly (SSTA) over the entire time period GHRSST data is available (2003-2013). SSTA is defined as the SST minus the seasonal and longer-frequency cycles. The seasonal cycle is defined as the average daily temperatures over the GHRSST time period. We then subtract the 13-month smoothed time series so that we isolate short timescale events. The temperatures are area-averaged over the locations of the six inshore stations of the ACT line. Data below the red line represent times identified as cold events. The green dot shows the data corresponding to the meander-induced cold event of April 2010 while the black dot shows the data corresponding to the wind-induced cold event of February 2013.
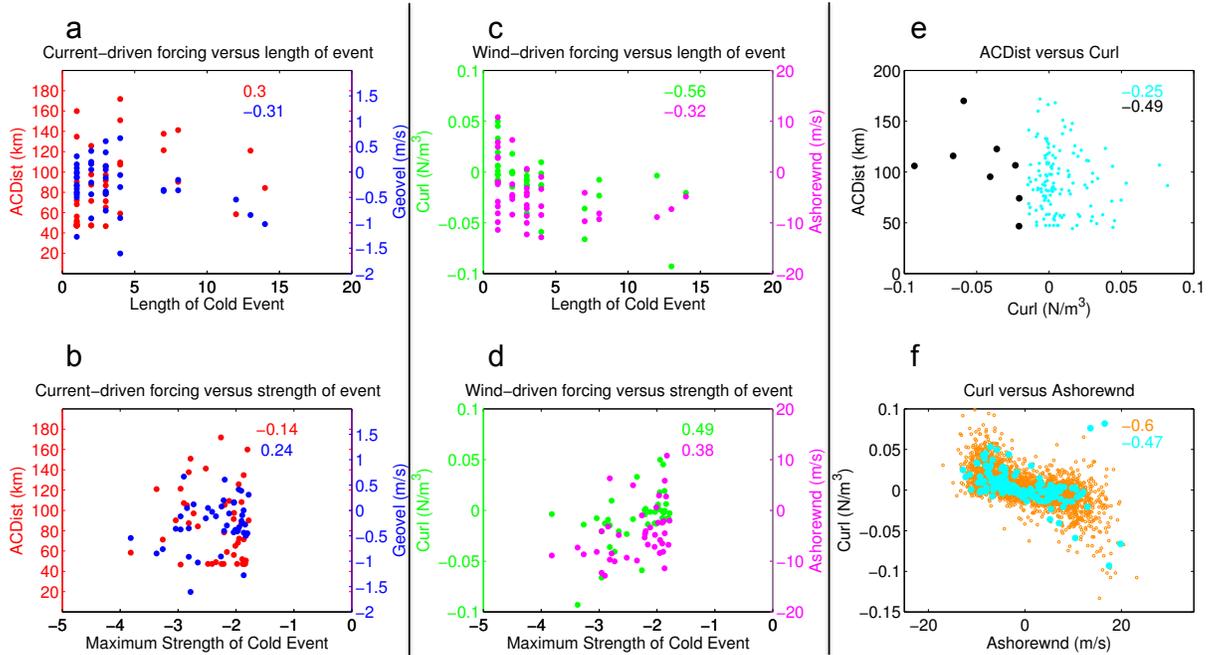
Figure 4.5: Six panels showing the four forcing mechanisms vs. length and strength of cold events and forcing mechanism dependencies. Panels a and b show current-driven forcing (ACDist in red and Geovel in blue) and panels c and d show wind-driven forcing (curl in green and ashorewnd in magenta). Panels a and c compare these forcings to the length of cold events and panels b and d compare these forcings to the maximum strength of a cold event. Correlations between forcings and length or maximum strength of cold event are given in the top right of panels a, b, d and e, with the colors corresponding to the different forcing. The total number of cold events is 47, so that a correlation of 0.372 or greater is significant at the 99% level, a correlation of 0.288 or greater is significant at the 95% level and a correlation of 0.243 or greater is significant at the 90% level. Panel e compares ACDist and curl while panel f compares alongshore wind and curl. For panels e and f, cold event days are show in cyan. In panel e, black dots are strong curl events and in panel f, orange points show all data points.
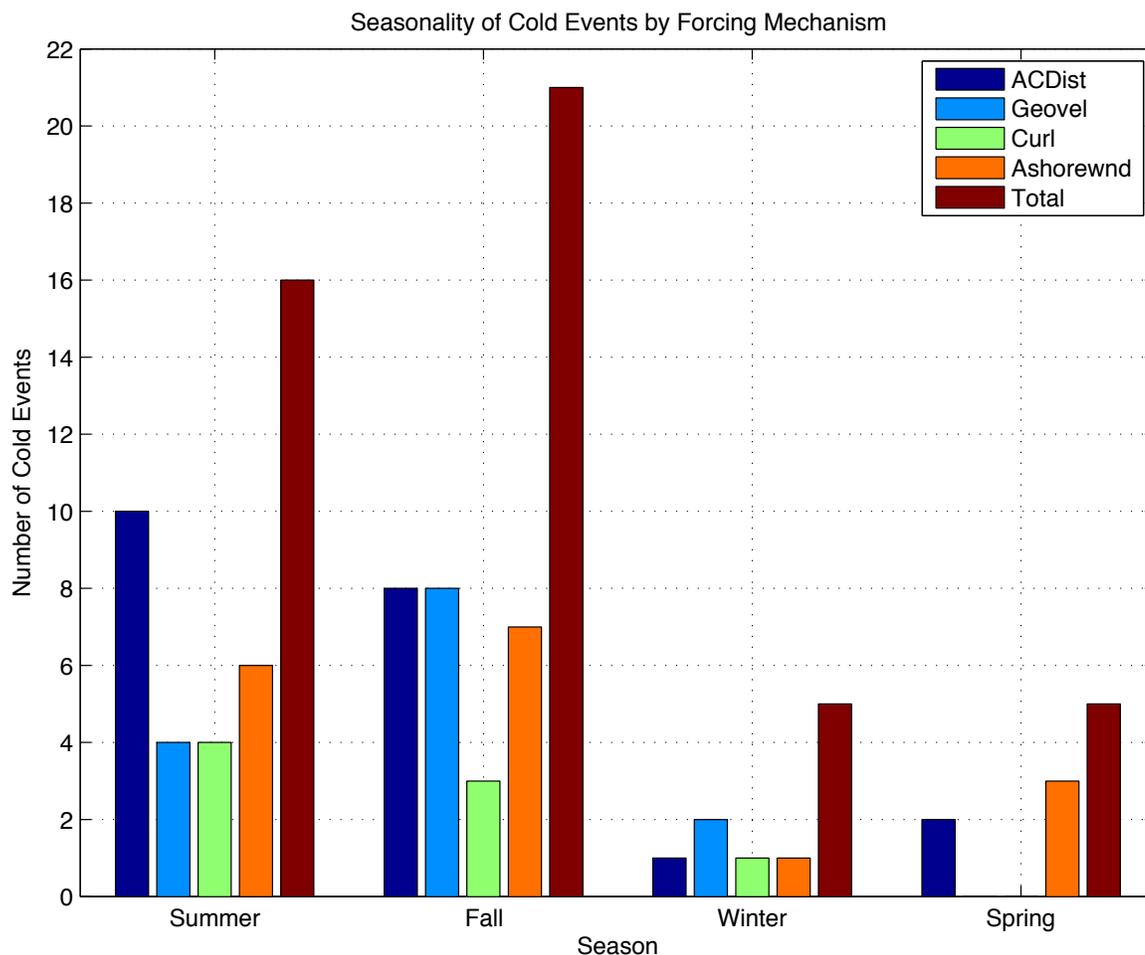
Figure 4.6: Bar graph showing the seasonality of cold events and forcing mechanisms. We separate the number of cold events during: Austral Summer (December, January and February); Austral Fall (March, April and May); Austral Winter (June, July and August); and Austral Spring (September, October and November). The number of cold events where one of the forcing mechanisms is strong, as defined in the text, is given by the first four bars for each season. From left to right, the histogram shows the number of cold events with strong ACDist, Geovel, Curl and Ashorewnd. The last bar for each season gives the total number of cold events for that season.
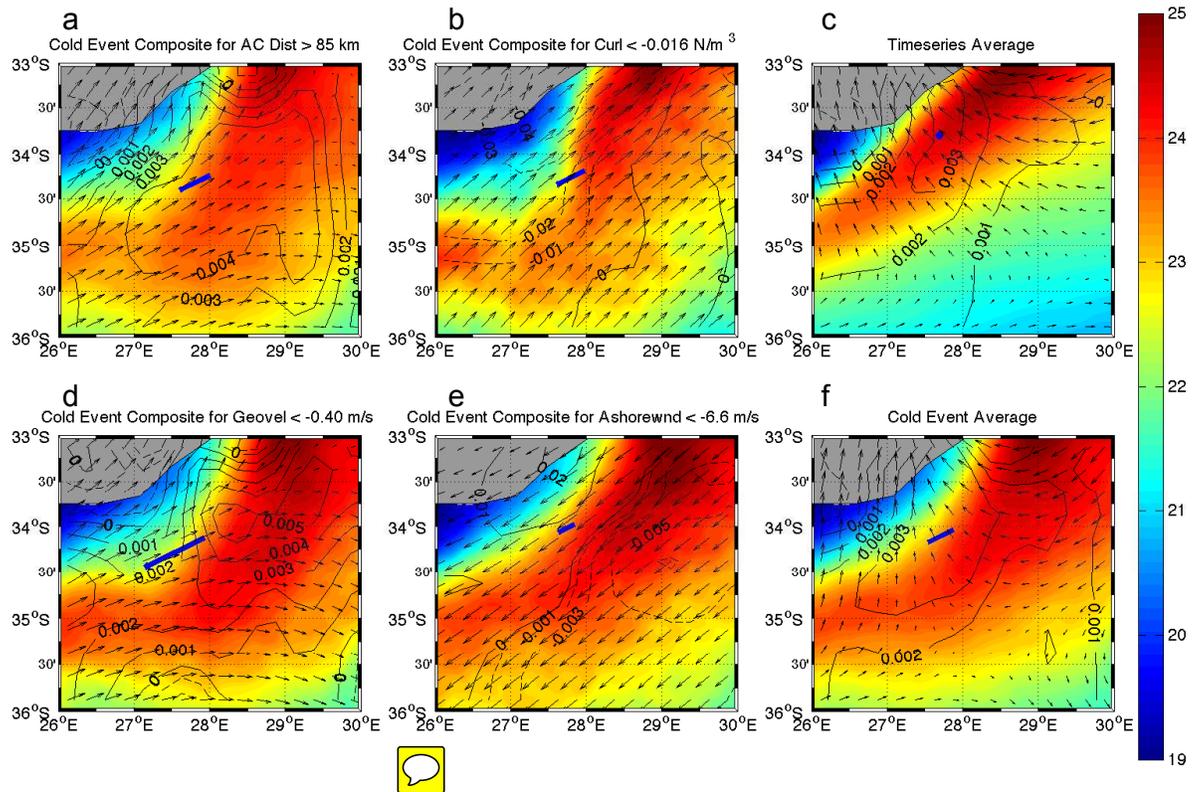
Figure 4.7: Six panels showing composites during times of strong forcing as well as cold events and the timeseries average. Colors are GHRSST SST using the colorbar on the right. The vectors show alongshore wind. The contours show wind stress curl, with negative values dashed and positive values solid. The blue vector shows the location and strength of the AC core. Top left panel shows composite for AC distance greater than 85 km, which is one standard deviation above the mean for AC distance. Top middle shows composite for curl less than -0.016 N/m^3, which is one standard deviation below the mean for wind stress curl. The bottom left panel shows composite for geostrophic velocity less than -0.40 m/s, which is one standard deviation below the mean. The bottom middle panel shows composite for cross-track wind less than -6.6 m/s, which is one standard deviation below the mean for cross-track wind. The top right panel shows average values for the entire timeseries while the bottom right panel shows average values during cold events.

Chapter 5

Conclusions

This work presents the first ever full-depth hydrographic and direct velocity observations of a solitary meander in the Agulhas Current. As discussed in Chapter 2, these data allow us to determine how solitary meanders effect the velocity structure and transport of the current. In Chapter 3, we examine how solitary meanders effect the instantaneous water mass distribution of the current. In particular, we investigate whether solitary meanders are able to cause upwelling, cross-frontal mixing and diapycnal transport as has been seen within meanders of other western boundary currents. Finally, in Chapter 4, we explore the broader implications of meandering by identifying their ability, as well as other local forcing mechanisms, to force cold events over an 11-year period. Here, we summarize the main conclusions from each of these three chapters as well as offer some perspective on their broader implications.

As the current meanders offshore, its core both broadens and weakens. These two effects compensate for each other so that the transport of the current is maintained during meandering. This disagrees with both model studies that show meanders increase AC transport (Biastoch et al., 2009), and observations at 32°S that show AC transports reducing by 15-25 Sv during a meander (Bryden et al., 2005). At the same time, the Eulerian transport across the line decreases significantly due to the

development of an inshore countercurrent. This inshore countercurrent represents a barotropic change to the AC since the transport per unit depth is unchanged. Our analysis of the horizontal momentum equations shows that, like the meandering Gulf Stream (Johns et al., 1989), the meandering Agulhas current is in geostrophic balance. However, its fast propagation biases these measurements since the sloping isopycnals of the current are moving relative to our hydrographic stations. Hence, LADCP measurements are necessary to study the structure of the meandering current.

Since the current broadens as it meanders, it loses the asymmetry that is characteristic of its non-meandering state. When the current is not meandering, its inshore relative vorticity is much greater than its offshore. During a meander, these values are comparable. The main changes in total potential vorticity between the meandering and non-meandering current are due to the input of cyclonic vorticity inshore that causes thinning isopycnal thermocline layers over the continental slope. The thinner thermocline layer during the meander also uplifts and 0.25 fresher and 1°C cooler waters appear above the layer and 0.25 saltier and 1 °C warmer waters appear above this layer. These changes suggest that the meander is causing diapycnal fluxes out of the thermocline layer. We introduce a new streamwise coordinate system, based on cumulative transport, to determine how much of these apparent diapycnal fluxes are due to kinematic changes as the current shifts offshore and broadens. We also compare to both non-meander lines to assess how much of the changes are due to seasonal variability. Our streamwise coordinate system shows that approximately 60% of the observed temperature-salinity changes below the thermocline are due to diapycnal fluxes. Changes above the thermocline are muddled by seasonal variability, but are likely also the result of diapycnal fluxes.

We find that the Agulhas Current's large barotropic component maintains a deep kinematic steering level that restricts cross-frontal mixing regardless of meandering.

Although we find some evidence for increased cross-frontal mixing during the meander, it is statistically insignificant. Possibly our results from a single-meander event cannot be generalized. Future research is needed to determine whether meander events of a different size or stage of development initiate significant mixing. Although cross-frontal fluxes are not significantly enhanced, our streamwise analysis suggests that there is enhanced diapycnal fluxes during a meander. This suggests that mixing during the meander is enhanced in the cross-frontal direction on either side of the current, even though mixing across the current core is suppressed.

The passing meander cools inshore SST 5°C over just two days coincident with an uplift of South Indian Central Water from the continental slope to the continental shelf. Our analysis of the material derivative of temperature shows that this temperature change is mostly due to upwelling, with an additional possible contribution from horizontal advection of Agulhas Bank waters. We find that the speed of upwelling, at least 13.3 m per day but likely as much as 66.5-133 m per day, is short-lived but large. Upwelling of 66.5 m per day would be more than twice the vertical velocities observed in the Benguela current (26 m per day) and are comparable to those observed in the Canary Current (86 m per day) (Merino et al., 2004).

We find that upwelling events inshore of the Agulhas Current at 34°S can be forced by both wind and current mechanisms. Regardless of forcing mechanism, upwelling events lift South Indian Central Water onto the continental shelf and cool shelf waters as much as 9°C. This is similar to the upwelling events of the Brazil Current that bring South Atlantic Central Water onto the shelf and can be forced by either current or wind mechanisms (Campos et al., 2000).

We identify cold events between 2003 and 2014 that significantly correlate with local forcing mechanisms: alongshore wind speed, wind stress curl, Agulhas Current strength and meandering. We find an average of 4 events lasting 3.5 days each year.

Our identified cold events likely do not last long enough to enter the euphotic zone and support sustained biological productivity (Chavez and Toggweiler, 1994).Their main importance, then, is likely related to their ability to advect surface waters that may be rich in larvae and represent population sinks (Porri et al., 2014). Contrary to what our in-situ data suggest, neither cold event length or strength depend on their forcing mechanism. Cold event frequency peaks in austral summer and fall, when prevailing winds are upwelling-favorable. A similar seasonality was found in the Brazil Current (Campos et al., 2000).

Our four forcing mechanisms are not independent since wind stress curl is found to be highly dependent on both meandering and alongshore winds. We find that 75% of wind stress curl-forced events occur during meandering. We find that the correlation between the crosswind SST gradient and the local wind stress curl is significant, suggesting that the frontal variability of meanders is forcing local wind stress curl. The cold events with strong wind stress curl and meandering are the coldest. We believe that after meanders are fully developed, they force a local wind stress curl that further enhances upwelling. This is observed during our April 2010 in-situ meander event, where strong upwelling-favorable wind stress curl develops for the last two days of the cold event. Wind stress curl is also significantly anticorrelated with alongshore wind. We attribute this to the general pattern of wind speed decreasing away from the coast such that upwelling-favorable wind stress curl is due to downwelling-favorable alongshore winds and vice versa.

Current-driven cold events are 3 times as common as wind-driven cold events, so that the structure of the average cold event has upwelling-favorable current anomalies but neutral/downwelling-favorable winds. Although they are less frequent, wind-driven cold events are slightly stronger. Meanders account for almost half of cold events, and increased current strength explains roughly one quarter. Alongshore

winds account for 18% of cold events, and wind stress curl explains just 5%, and is highly dependent on meandering and alongshore winds. Ultimately, our identified local forcing mechanisms explain 81% of cold event days and 93% of cold events. Unlike the Brazil Current where 100% of upwelling events are linked to either local wind or current effects (Aguiar et al., 2014), the Agulhas Current is a more complex system with some upwelling events likely due to remote forcing mechanisms such as the influence of coastal-trapped waves (Goschen et al., 2012).

References

Aguiar, A., M. Cirano, J. Pereira, and M. Marta-Almeida, 2014: Upwelling processes along a western boundary current in the abrolhos–campos region of brazil. *Continental Shelf Research*, **85**, 42–59. 39, 74, 89

Atkinson, L., J. BLANTON, W. CHANDLER, and T. LEE, 1983: Climatology of the southeastern united states continental shelf waters. *Journal of Geophysical Research*, **88**, 4705–4718. 11, 39, 63

Atlas, R., R. N. Hoffman, J. Ardizzone, S. M. Leidner, J. C. Jusem, D. K. Smith, and D. Gombos, 2011: A cross-calibrated, multiplatform ocean surface wind velocity product for meteorological and oceanographic applications. *Bulletin of the American Meteorological Society*, **92 (2)**, 157–174. 67

Backeberg, B., L. Bertino, and J. Johannessen, 2009: Evaluating two numerical advection schemes in hycom for eddy-resolving modelling of the agulhas current. *Ocean Sci*, **5 (2)**, 173–190. 7, 12

Beal, L., 2009: A time series of agulhas undercurrent transport. *Journal of physical oceanography*, **39 (10)**, 2436–2450. 1, 5, 12

Beal, L. and H. Bryden, 1999: The velocity and vorticity structure of the agulhas current at 32 s. *Journal of Geophysical Research*, **104 (C3)**, 5151–5176. 5, 20, 26, 27

Beal, L., T. Chereskin, Y. Lenn, and S. Elipot, 2006: The sources and mixing characteristics of the agulhas current. *Journal of physical oceanography*, **36 (11)**, 2060–2074. 9, 10, 39, 46, 47, 69

Beal, L., W. De Ruijter, A. Biastoch, R. Zahn, et al., 2011: On the role of the agulhas system in ocean circulation and climate. *Nature*, **472 (7344)**, 429–436. 2, 7

Beckley, L. and R. Van Ballegooyen, 1992: Oceanographic conditions during three ichthyoplankton surveys of the agulhas current in 1990/91. *South African Journal of Marine Science*, **12 (1)**, 83–93. 8

Biastoch, A., L. Beal, J. Lutjeharms, and T. Casal, 2009: Variability and coherence of the agulhas undercurrent in a high-resolution ocean general circulation model. *Journal of physical oceanography*, **39 (10)**, 2417–2435. 5, 7, 12, 16, 17, 85

Biastoch, A., C. Böning, J. Getzlaff, J. Molines, and G. Madec, 2008: Causes of interannual-decadal variability in the meridional overturning circulation of the mid-latitude north atlantic ocean. *Journal of Climate*, **21 (24)**, 6599–6615. 7

Bower, A., H. Rossby, and J. Lillibridge, 1985: The gulf stream-barrier or blender? *Journal of Physical Oceanography*, **15 (1)**, 24–32. 10, 39, 46, 63

Brandini, F., 1990: Hydrography and characteristics of the phytoplankton in shelf and oceanic waters off southeastern brazil during winter (july/august 1982) and summer (february/march 1984). *Hydrobiologia*, **196 (2)**, 111–148. 11, 63, 64

Bryden, H., L. Beal, and L. Duncan, 2005: Structure and transport of the agulhas current and its temporal variability. *Journal of oceanography*, **61 (3)**, 479–492. 1, 2, 4, 5, 12, 16, 17, 25, 28, 29, 40, 45, 63, 85

Campos, E., D. Velhote, and I. da Silveira, 2000: Shelf break upwelling driven by brazil current cyclonic meanders. *Geophysical Research Letters*, **27 (6)**, 751–754. 11, 39, 63, 64, 75, 87, 88

Casal, T. G., L. M. Beal, R. Lumpkin, and W. E. Johns, 2009: Structure and down-stream evolution of the agulhas current system during a quasi-synoptic survey in february–march 2003. *Journal of Geophysical Research: Oceans (1978–2012)*, **114 (C3)**. 29

Castelao, R., E. Cannipos, and J. Miller, 2004: A modelling study of coastal upwelling driven by wind and meanders of the brazil current. *Journal of coastal research*, **20 (3)**, 662–671. 11, 12, 64, 72

Castelao, R. M. and J. A. Barth, 2006: Upwelling around cabo frio, brazil: The importance of wind stress curl. *Geophysical research letters*, **33 (3)**. 12, 64

Castro, B. d. and L. d. Miranda, 1998: Physical oceanography of the western atlantic continental shelf located between 4 n and 34 s. *The sea*, **11**, 209–251. 11, 63

Chavez, F. and J. Toggweiler, 1994: Physical estimates of global new production: The up-welling contribution. *Wokshop. Berlin (Germany). 25Á30 Sep 1994.* 75, 88

Chelton, D. B., M. G. Schlax, and R. M. Samelson, 2007: Summertime Coupling between Sea Surface Temperature and Wind Stress in the California Current System. *Journal of Physical Oceanography*, **37 (3)**, 495–517. 72

Churchill, J. H., P. C. Cornillon, and G. W. Milkowski, 1986: A cyclonic eddy and shelf-slope water exchange associated with a gulf stream warm-core ring. *Journal of Geophysical Research: Oceans (1978–2012)*, **91 (C8)**, 9615–9623. 11, 63

Darbyshire, M., 1966: The surface waters near the coasts of southern africa. **13 (1)**, 57–81. 10, 46

de Ruijter, W., P. van Leeuwen, and J. Lutjeharms, 1999: Generation and evolution of natal pulses: Solitary meanders in the agulhas current. *Journal of physical oceanography*, **29 (12)**, 3043–3055. 3, 4, 5, 16, 19, 40

Drazin, P. and R. Johnson, 1989: *Solitons: An Introduction*. Cambridge Texts in Applied Mathematics, Cambridge University Press, URL `http://books.google.it/books?id=HPmbIDk2u-gC`. 4

Flierl, G. and C. Davis, 1993: Biological effects of gulf stream meandering. *Journal of Marine Research*, **51 (3)**, 529–560. 12, 64

Garratt, P., 1988: Notes on seasonal abundance and spawning of some important offshore linefish in natal and transkei waters, southern africa. *South African Journal of Marine Science*, **7 (1)**, 1–8. 8

Gawarkiewicz, G., F. Bahr, R. C. Beardsley, and K. H. Brink, 2001: Interaction of a slope eddy with the shelfbreak front in the middle atlantic bight*. *Journal of physical oceanography*, **31 (9)**, 2783–2796. 11, 64

Gordon, A., 1986: Interocean exchange of thermocline water. *J. geophys. Res*, **91 (C4)**, 5037–5046. 6, 16

Goschen, W. and E. Schumann, 1990: Agulhas current variability and inshore structures off the cape province, south africa. *Journal of Geophysical Research*, **95 (C1)**, 667–678. 4

Goschen, W., E. Schumann, K. Bernard, S. Bailey, and S. Deyzel, 2012: Upwelling and ocean structures off algoa bay and the south-east coast of south africa. *African Journal of Marine Science*, **34 (4)**, 525–536. 65, 66, 71, 72, 74, 89

Gründlingh, M., 1980: On the volume transport of the agulhas current. *Deep Sea Research Part A. Oceanographic Research Papers*, **27 (7)**, 557–563. 2

Gründlingh, M., 1983: On the course of the agulhas current. *S. Afr. Geogr. J*, **65 (1)**, 49–57. 2

Gründlingh, M., 1992: Agulhas current meanders: review and case study. *South African geographical journal*, **74 (1)**, 19–28. 3, 8, 16

Hanawa, K. and L. D. Talley, 2001: Mode waters. *International Geophysics Series*, **77**, 373–386. 28

Hansen, D. V., 1970: Gulf stream meanders between cape hatteras and the grand banks. *Deep Sea Research and Oceanographic Abstracts*, **17 (3)**, 495–511. 39

Harris, T., 1972: Sources of the agulhas current in the spring of 1964. *Deep-Sea Research*, **19**, 633–650. 2, 10, 46

Heydorn, A., et al., 1978: Ecology of the agulhas current region: An assessment of biological responses to environmental parameters in the south-west indian ocean. *Transactions of the Royal Society of South Africa*, **43 (2)**, 151–190. 8

Hoffman, R., S. Leidner, J. Henderson, R. Atlas, J. Ardizzone, and S. Bloom, 2003: A two-dimensional variational analysis method for nscat ambiguity removal: Methodology, sensitivity, and tuning. *Journal of Atmospheric and Oceanic Technology*, **20 (5)**, 585–605. 68

Hutchings, L., L. Beckley, M. Griffiths, M. Roberts, S. Sundby, and C. Van Der Lingen, 2002: Spawning on the edge: spawning grounds and nursery areas around the southern african coastline. *Marine and Freshwater Research*, **53 (2)**, 307–318. 63

Huthnance, J. M., 1995: Circulation, exchange and water masses at the ocean margin: the role of physical processes at the shelf edge. *Progress in Oceanography*, **35 (4)**, 353–431. 39

Jackett, D. R. and T. J. McDougall, 1997: A neutral density variable for the world's oceans. *Journal of Physical Oceanography*, **27 (2)**, 237–263. 25, 68

Jackson, J. M., L. Rainville, M. J. Roberts, C. D. McQuaid, and J. R. Lutjeharms, 2012: Mesoscale bio-physical interactions between the agulhas current and the agulhas bank, south africa. *Continental Shelf Research*, **49**, 10–24. 40, 64

Johns, E., D. Watts, and H. Rossby, 1989: A test of geostrophy in the gulf stream. *Journal of Geophysical Research*, **94 (C3)**, 3211–3222. 6, 23, 86

Joyce, T. M., K. A. Kelly, D. M. Schubert, and M. J. Caruso, 1990: Shipboard and altimetric studies of rapid gulf stream variability between cape cod and bermuda. *Deep Sea Research Part A. Oceanographic Research Papers*, **37 (6)**, 897–910. 22

Jury, M., H. Valentine, and J. Lutjeharms, 1993: Influence of the agulhas current on summer rainfall along the southeast coast of south africa. *Journal of applied meteorology*, **32 (7)**, 1282–1287. 8, 16

Krug, M. and J. Tournadre, 2012: Satellite observations of an annual cycle in the agulhas current. *Geophysical Research Letters*, **39 (15)**. 67

Krug, M., J. Tournadre, and F. Dufois, 2014: Interactions between the agulhas current and the eastern margin of the agulhas bank. *Continental Shelf Research*, **81**, 67–79. 40

Large, W. and S. Pond, 1981: Open ocean momentum flux measurements in moderate to strong winds. *Journal of physical oceanography*, **11 (3)**, 324–336. 68

Leber, G. M. and L. M. Beal, 2014: Evidence that agulhas current transport is maintained during a meander. *Journal of Geophysical Research: Oceans*, **119 (6)**, 3806–3817. 40, 42, 47, 49, 69

Leber, G. M. and L. M. Beal, 2015: Local water mass modifications by a solitary meander in the agulhas current, in review. *Journal of Geophysical Research: Oceans*, **TBD (TBD)**, TBD. 69

Lee, T., L. Atkinson, and R. Legeckis, 1981: Observations of a gulf stream frontal eddy on the georgia continental shelf, april 1977. *Deep Sea Research Part A. Oceanographic Research Papers*, **28 (4)**, 347–378. 12, 64

Lee, T. N. and E. Williams, 1988: Wind-forced transport fluctuations of the florida current. *Journal of Physical Oceanography*, **18 (7)**, 937–946. 73

Lutjeharms, J., O. Boebel, and H. Rossby, 2003: Agulhas cyclones. *Deep Sea Research Part II: Topical Studies in Oceanography*, **50 (1)**, 13–34. 4, 6, 12, 16, 40

Lutjeharms, J., O. Boebel, P. van der Vaart, W. de Ruijter, T. Rossby, and H. Bryden, 2001: Evidence that the natal pulse involves the agulhas current to its full depth. *Geophysical research letters*, **28 (18)**, 3449–3452. 5, 16, 48

Lutjeharms, J., R. Catzel, and H. Valentine, 1989: Eddies and other boundary phenomena of the agulhas current. *Continental Shelf Research*, **9 (7)**, 597–616. 2, 3, 4, 16

Lutjeharms, J. and A. Connell, 1989: The natal pulse and inshore counter currents off the south african east coast. *S. Afr. J. Sci*, **85 (8)**, 533–535. 16, 25

Lutjeharms, J. and W. De Ruijter, 1996: The influence of the agulhas current on the adjacent coastal ocean: possible impacts of climate change. *Journal of marine systems*, **7 (2)**, 321–336. 7, 8, 16

Lutjeharms, J. and H. Roberts, 1988: The natal pulse: An extreme transient on the agulhas current. *Journal of Geophysical Research*, **93 (C1)**, 631–645. 3, 4, 8, 19, 43

Lutjeharms, J. R. E., 2006: *The Agulhas Current*. Springer. 2

Massey Jr, F. J., 1951: The kolmogorov-smirnov test for goodness of fit. *Journal of the American statistical Association*, **46 (253)**, 68–78. 47

McClain, C. R. and L. P. Atkinson, 1985: A note on the Charleston Gyre. *J. Geophys. Res.*, **90**, 11 857–11 861. 71

Merino, M., A. Monreal, and C. Duarte, 2004: Ocean currents and their impact on marine life. *Marine Ecology, CM Duarte, ed., in Encyclopedia of Life Support Systems (EOLSS), developed under the auspices of UNESCO, Eolss Publishers, Oxford, UK*, 1À22. 51, 87

Miller, J. L. and T. N. Lee, 1995: Gulf stream meanders in the south atlantic bight: 1. scaling and energetics. *Journal of Geophysical Research*, **100 (C4)**, 6687–6704. 11, 39, 63

Okkonen, S., T. Weingartner, S. Danielson, D. Musgrave, and G. Schmidt, 2003: Satellite and hydrographic observations of eddy-induced shelf-slope exchange in the northwestern gulf of alaska. *Journal of Geophysical Research*, **108 (C2)**, 3033. 11, 64

Olson, D. and R. Evans, 1986: Rings of the agulhas current. *Deep Sea Research Part A. Oceanographic Research Papers*, **33 (1)**, 27–42. 1, 6

Olson, D. B., 2001: Biophysical dynamics of western transition zones: a preliminary synthesis. *Fisheries Oceanography*, **10 (2)**, 133–150. 39

Olson, D. B., 2002: Biophysical dynamics of ocean fronts, in: Biological-physical interactions in the sea, A.R. Robinson, J.J. McCarthy and B. Rothschild (eds.). *The Sea*, **12**, 187–218. 12, 64

Owens, W., 1984: A synoptic and statistical description of the gulf stream and subtropical gyre using sofar floats. *Journal of physical oceanography*, **14 (1)**, 104–113. 10, 46, 47

Pedlosky, J., 1986: *Geophysical Fluid Dynamics*. Springer-Verlag. 26

Penven, P., J. Lutjeharms, and P. Florenchie, 2006: Madagascar: A pacemaker for the agulhas current system? *Geophysical research letters*, **33 (17)**, L17 609. 6, 7, 16

Pichevin, T., D. Nof, and J. Lutjeharms, 1999: Why are there agulhas rings? *Journal of physical oceanography*, **29 (4)**, 693–707. 5, 7, 16

Porri, F., J. M. Jackson, C. E. Von der Meden, N. Weidberg, and C. D. McQuaid, 2014: The effect of mesoscale oceanographic features on the distribution of mussel larvae along the south coast of south africa. *Journal of Marine Systems*, **132**, 162–173. 39, 63, 64, 71, 75, 88

Rio, M., S. Guinehut, and G. Larnicol, 2011: New cnes-cls09 global mean dynamic topography computed from the combination of grace data, altimetry, and in situ measurements. *Journal of Geophysical Research: Oceans (1978–2012)*, **116 (C7)**. 18, 67

Rodríguez-Santana, A., J. Pelegrí, P. Sangra, and A. Marrero-Díaz, 1999: Diapycnal mixing in gulf stream meanders. *Journal of geophysical research*, **104 (C11)**, 25 891–25. 10, 11, 39

Rouault, M. and P. Penven, 2011: New perspectives on natal pulses from satellite observations. *Journal of Geophysical Research*, **116 (C7)**, C07 013. 3, 4, 6, 8, 12, 39, 40

Roughan, M. and J. Middleton, 2002: A comparison of observed upwelling mechanisms off the east coast of australia. *Continental Shelf Research*, **22 (17)**, 2551–2572. 64

Schouten, M., W. de Ruijter, and P. van Leeuwen, 2002: Upstream control of agulhas ring shedding. *Journal of Geophysical Research*, **107 (C8)**, 3109. 3, 4, 6, 16

Shaw, P. and H. Rossby, 1984: Towards a lagrangian description of the gulf stream. *Journal of physical oceanography*, **14**, 528–540. 10, 39, 46

Smith, R., 1995: The physical processes of coastal ocean upwelling systems. *ENVIRONMENTAL SCIENCES RESEARCH REPORT ES*, **18**, 39–64. 64

Stabeno, P. and P. Van Meurs, 1999: Evidence of episodic on-shelf flow in the southeastern bering sea. *Journal of Geophysical Research: Oceans (1978–2012)*, **104 (C12)**, 29 715–29 720. 11, 63

Stramma, L. and J. Lutjeharms, 1997: The flow field of the subtropical gyre of the south indian ocean. *Journal of Geophysical Research*, **102 (C3)**, 5513–5530. 9

Thurnherr, A., 2010: A practical assessment of the errors associated with full-depth ladcp profiles obtained using teledyne rdi workhorse acoustic doppler current profilers. *Journal of Atmospheric and Oceanic Technology*, **27 (7)**, 1215–1227. 21

Toole, J. and B. Warren, 1993: A hydrographic section across the subtropical south indian ocean. *Deep Sea Research Part I: Oceanographic Research Papers*, **40 (10)**, 1973–2019. 9, 10, 46

Tsugawa, M. and H. Hasumi, 2010: Generation and growth mechanism of the natal pulse. *Journal of Physical Oceanography*, **40 (7)**, 1597–1612. 3, 4, 39

Valentine, H., J. Lutjeharms, and G. Brundrit, 1993: The water masses and volumetry of the southern agulhas current region. *Deep Sea Research Part I: Oceanographic Research Papers*, **40 (6)**, 1285–1305. 9

van Leeuwen, P., W. de Ruijter, and J. Lutjeharms, 2000: Natal pulses and the formation of agulhas rings. *Journal of Geophysical Research*, **105 (C3)**, 6425–6436. 6, 16

Vecchi, G. A., S.-P. Xie, and A. S. Fischer, 2004: Ocean-atmosphere covariability in the western arabian sea*. *Journal of climate*, **17 (6)**, 1213–1224. 72

Visbeck, M., 2002: Deep velocity profiling using lowered acoustic doppler current profilers: Bottom track and inverse solutions*. *Journal of Atmospheric and Oceanic Technology*, **19 (5)**, 794–807. 20, 29

Warren, B., 1981: Transindian hydrographic section at lat. 18 s: Property distributions and circulation in the south indian ocean. *Deep Sea Research Part A. Oceanographic Research Papers*, **28 (8)**, 759–788. 9

Weidberg, N., F. Porri, C. E. Von der Meden, J. M. Jackson, W. Goschen, and C. D. McQuaid, 2015: Mechanisms of nearshore retention and offshore export of mussel larvae over the agulhas bank. *Journal of Marine Systems*, **144**, 70–80. 64

Xie, J., J. Zhu, and Y. Li, 2008: Assessment and inter-comparison of five high-resolution sea surface temperature products in the shelf and coastal seas around china. *Continental Shelf Research*, **28 (10)**, 1286–1293. 41, 66